Effects of wind speed changes on wake instability of a wind turbine in a virtual wind tunnel using large eddy simulation

Jang-Oh Mo [1], Amanullah Choudhry [1*], Maziar Arjomandi [1], Richard Kelso [1], Young-Ho Lee [2]

[1] School of Mechanical Engineering, The University of Adelaide, South Australia 5005, Australia
[2] Division of Mechanical and Energy-System Engineering, Korea Maritime, Busan, 606-791, Korea

** Corresponding Author*

Email: amanullah.choudhry@adelaide.edu.au

Mobile Number: 0061-413032885

Effects of wind speed changes on wake instability of a wind turbine in a virtual wind tunnel using large eddy simulation

Jang-Oh Mo [1], Amanullah Choudhry [1*], Maziar Arjomandi [1], Richard Kelso [1], Young-Ho Lee [2]

[1] School of Mechanical Engineering, The University of Adelaide, South Australia 5005, Australia
[2] Division of Mechanical and Energy-System Engineering, Korea Maritime, Busan, 606-791, Korea

Abstract

Large Eddy Simulation (LES) of the NREL (National Renewable Energy Laboratory) Phase VI wind turbine inside a virtual wind tunnel, with the same test section as that of NASA Ames 24.4 m × 36.6 m, was carried out in order to analyse and better understand the wake instability and its breakdown behind the wind turbine. LES was performed using the commercial CFD software, ANSYS FLUENT, based on the dynamic Smagorinsky-Lilly model. The wind turbine was placed at a distance of two rotor diameters from the upstream boundary with a downstream domain of twenty rotor diameters in length The results of the simulation were compared with the experimental data published by the NREL and a good agreement was found between the two. Furthermore, the average turbulence intensities from the LES were compared with a semi-empirical model and very good agreement was observed, except for the regions of on-going wake instability and vortex breakdown. It was observed that the wake behind the wind turbine consists of a system of intense and stable rotating helical vortices. These vortices persisted for some distance downstream of the wind turbine and finally become unstable producing a sinuous shape. The downstream distance at which wake instability and vortex breakdown occur, was observed to be a function of the upstream wind speed. For example, for an upstream wind speed of 7 m/s, it was observed that the primary vortex structure became unstable at a downstream distance of four rotor diameters and complete breakdown occurred at approximately six rotor diameters. On the other hand, when the upstream wind speed was 15.1 m/s, wake instability occurred at approximately eleven rotor diameters downstream of the wind turbine and complete breakdown was observed at thirteen rotor diameters downstream of the wind turbine. Furthermore, it was observed that the turbulence intensity rapidly decreased during the process of wake instability and vortex breakdown; the location of the decrease is a function of the upstream wind speed. It is suggested that the distinction between the near and far wake can be identified as the average location between the start of the wake instability and the end of the process, at complete breakdown. Therefore the average location of this boundary is a function of the upstream wind speed. Hence for upstream wind speeds of 7 m/s, 10 m/s, 13.1 m/s and 15.1 m/s, the boundary between the near and far wake lies at five, seven, ten and twelve rotor diameters downstream respectively.

Keywords: Large eddy simulation; NREL Phase VI wind turbine; Wake instability; Vortex breakdown; Turbulence intensity; Virtual wind tunnel;

1. Introduction

A wind farm is a locally-clustered group of wind turbines at the same location used to produce electric power with the goal of zero carbon footprint. A large wind farm may consist of several hundred individual wind turbines, and cover an extended area of hundreds of square kilometers. There are many advantages to this commercial structure. In most countries, areas with commercially viable wind speeds are restricted to certain regions. This creates the necessity of concentrating as many wind turbines as possible in these regions to take advantage of the geographically-limited rich wind resources. The spatial concentration of several wind turbines also offers considerable advantages to the maintenance aspects of the operation since it is more cost-effective to maintain a large number of wind turbines in close proximity to each other (Hau, 2009).

Despite the commercial benefits of locally concentrated wind turbines, several drawbacks cannot be ignored with the arrangement. One of these disadvantages is that most wind turbines operate in the wakes of other wind turbines in a wind farm. Wakes behind horizontal axis wind turbines are turbulent flow structures with rotational motion being induced by the turbine blades, radial pressure gradients, tip vortices

and complex flows from the tower and the hub (Mo and Lee, 2011; Wagner et al., 1996). From the perspective of a wind farm optimal layout, the grouping of the wind turbines introduces two major issues: (1) A wind turbine operating in the wake of another turbine has a reduced power output because of the velocity deficit introduced by the upstream wind turbine during the process of momentum extraction from wind, and (2) Due to the large increase in the turbulence intensity (TI) in the wake and the consequent increase in the dynamic loads, the lifespan of the wind turbine blade operating in the wake is shortened (Barthelmie et al., 2009; Barthelmie et al., 2006; Chamorro and Porté-Agel, 2009; Sanderse, 2009) and therefore results in increased maintenance costs. Hence the study of wind turbine wakes is of paramount importance in order to increase the power output and operation life of the blades.

The wake of a wind turbine is typically divided into a near and a far wake (Vermeer et al., 2003). According to Vermeer et al. (2003), the former is the region from the turbine to approximately one rotor diameter downstream. This is the region where the turbine geometry determines the character of the flow field, affecting the performance of the turbine. In other words, it means that the rotor aerodynamics have an important impact on the near-wake structure. On the other hand, the far-wake is the region where the actual rotor shape is less important, but the focus lies on wake modelling, wake interference (wake farms), turbulence modelling and topographic effects (Sanderse, 2009; Vermeer et al., 2003).

Generally, the wake behind a wind turbine includes three kinds of vortices: bound lift-generating vortices (within the turbine blades), central or hub vortices and tip vortices (Hansen, 2001). The tip vortices are regarded as a system of intense rotating helical vortices which determine the basic dynamic behaviour of the far-wake. The tip vortices play the role of an efficient mixer, mixing the low velocity fluid in the wake with the high velocity fluid outside of it. The tip vortices become unstable and are reported to break down after approximately four rotor diameters downstream of the wind turbine for certain operating conditions of the turbine (Ainslie, 1985; Ainslie, 1988). The spacing between wind turbines is, therefore, of high importance. It has been observed that turbines placed in the regions of stable tip vortices have larger fatigue loads due to its severity as compared to operating in the region where tip vortex breakdown has already occurred (Okulov and Sorensen, 2004). Therefore, the correct determination of the wake effects play a pivotal role in the accurate placement of wind turbines and the spacing between the turbines in wind farms (Ivanell et al., 2007). For this reason, understanding of the turbulent wake behind a wind turbine has been the subject of research, both experimentally and numerically, over the last few decades. However, to the best of the authors' knowledge, most experiments have been performed at rather low Reynolds numbers, with only three cases exceeding a Reynolds number of 300,000 (Aderson et al., 1982; de Vries, 1979; Shimizu and Kamada, 2001). On the other hand, several numerical approaches reviewed by Vermeer et al. (2003) and Crespo et al. (1985) have been adopted to study wind turbine wakes. The work presented here is a continuation of the UPMWAKE model proposed by Crespo et al. (1985) and Crespo and Hernández (1989), which were developed based on the $k-\varepsilon$ closure methods and the explicit algebraic models for predicting the components of the turbulent stress tensor, as proposed by Gómez-Elvira et al. (2005). However, in all these methods, the Reynolds-Averaged Navier Stokes (RANS) method was used over all the turbulence scales and thus made it difficult to accurately predict the turbulent characteristics of the wake. Other semi-empirical methods like the Lissaman model (Lissaman, 1977; Lissaman et al., 1982) and its derivatives (Vermeulen et al., 1981) and the Risø model (Jensen, 1983; Katic et al., 1986) are based on using a near-Gaussian shape and a top-hat shape for the velocity deficits, respectively. As the results of these assumptions, certain details in the flow field around the turbine are neglected and the wakes are assumed to expand linearly with distance. A number of attempts have been made to establish more accurate wake models. However, so far advanced and detailed wake models, even when including an explicit representation of turbulence and its impact on the wake expansion, have not been able to produce significantly improved predictions (Barthelmie et al., 2006). Similarly, a number of researchers have used CFD, based on the RANS equations to acquire comparatively fast results (Menter et al., 2006; Potsdam and Mavriplis, 2009; Sørensen et al., 2002). Others have used LES to simulate the wake flows without the turbines, combined with the actuator line and disc methodologies (Wu and Porté-Agel, 2011). However, both these approaches have their limitations and do not yield the full details of the wake.

Therefore, in this research, Large Eddy Simulation (LES) has been used as the tool to investigate the details of the wind turbine wake, since all unsteady oscillations in the flow larger than the grid size can be determined consequently yielding the details of the turbulent characteristics of the wake. The NREL Phase VI wind turbine has been simulated, using the commercial CFD code, ANSYS FLUENT 13.0, inside a virtual wind tunnel with the same test section dimensions as that of the NASA Ames 24.4 m x 36.6 m wind tunnel. This was done in order to enable the validation of the simulation method, by comparing the pressure coefficients at different blade sections with the results published by the NREL.

The objective of this research was to understand and present the turbulent wake characteristics of the wind turbine. This includes in particular the distribution of the overall wake structure, including wake instability and its breakdown, the relationship between the wake structure and the TI change, the turbulent TI characteristics in both pre- and post-stall states, and the velocity deficit and recovery downstream of the wind turbine. Furthermore, comparisons have been made between the turbulence intensities obtained using semi-empirical models and those computed through LES. Therefore, in addition to the detailed understanding of the turbulent flow structures in

the wakes of wind turbines, the outcomes of this research can also be used for determining the overall efficiency losses of wind farms and for the establishment of guidelines for designing the layouts of large wind farms.

2. Numerical Simulation

2.1 Specifications of the NREL Phase VI wind turbine

In May 2000, NREL successfully completed analysis of the Phase VI wind turbine in the NASA Ames 24.4 m x 36.6 m wind tunnel. The details of the experiment and the results were then released on the NREL website (Web reference [1]) in order to verify the performance of commercially available analytical codes developed around the world. The present study also uses the Phase VI wind turbine for CFD simulations since the required geometrical data and the test results are publically available and can be accessed easily. The NREL Phase VI wind turbine is a stall-regulated wind turbine producing a rated output power of 19.8 kW. The experimental and computational models are shown in Fig. 1 and the details of the turbine are shown in Table 1. For the case considered in the present study, the twist angles are relative to the zero twist at the 0.75 span, and the blade is twisted from 18.074° at the root up to -1.816° at the tip. The turbine blade consists of the S809 airfoil with a thickness to chord ratio of 0.21. This airfoil was specifically designed to be less sensitive to the surface roughness at the leading edge of the wind turbine blade, in order to improve the turbine output power (Hand et al., 2001 ; Simms et al., 2001).

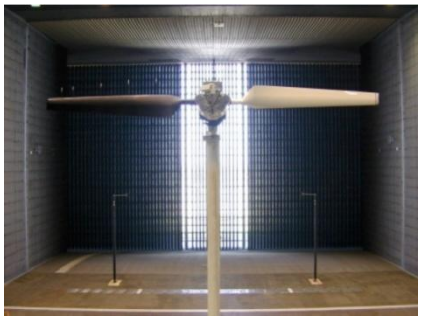

(a) NREL Phase VI wind turbine in the NASA-Ames 24.4 m by 36.6 m wind tunnel (Web reference [1]).

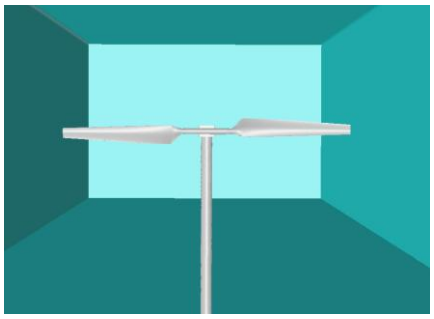

(b) CFD model of the turbine in a numerical wind tunnel.

Fig. 1 The NREL Phase VI wind turbine (a) and the developed numerical model (b).

Table 1. Specifications of NREL Phase VI wind turbine.

Number of blades Z	2
Rotor diameter d	10.058 m
Rotor radius R (d/2)	5.029
Rotational speed N	71.9 rpm
Cut-in wind speed V_c	6 m/s
Rated power	19.8 kW
Power regulation	stall
Rotational direction	CW
Global pitch angle	3°
Tower height h	11.5 m

2.2 Computational mesh

The computational domain has a height of 24.4 m and a width of 36.6 m, corresponding to the cross section of the NASA-Ames 24.4 m x 36.6 m wind tunnel, with a length of 221.3 m in the streamwise direction. This length includes two rotor diameters upstream of the turbine and twenty rotor diameter aft of the turbine as shown in Fig. 2. The wind turbine has a tower height of 11.5m and is placed approximately in the middle of the wind tunnel at a distance of 2d from the upwind boundary. The wind turbine blades are operating under uniform velocity

conditions, and therefore, the boundary layer velocity profile, such as that observed in open atmosphere, was not specified at the inlet. According to the NREL report (Simms, 2001), the test section size was a crucial factor in the selection of this particular wind tunnel for the subject experiment since it provided a minimal blockage for the rotor.

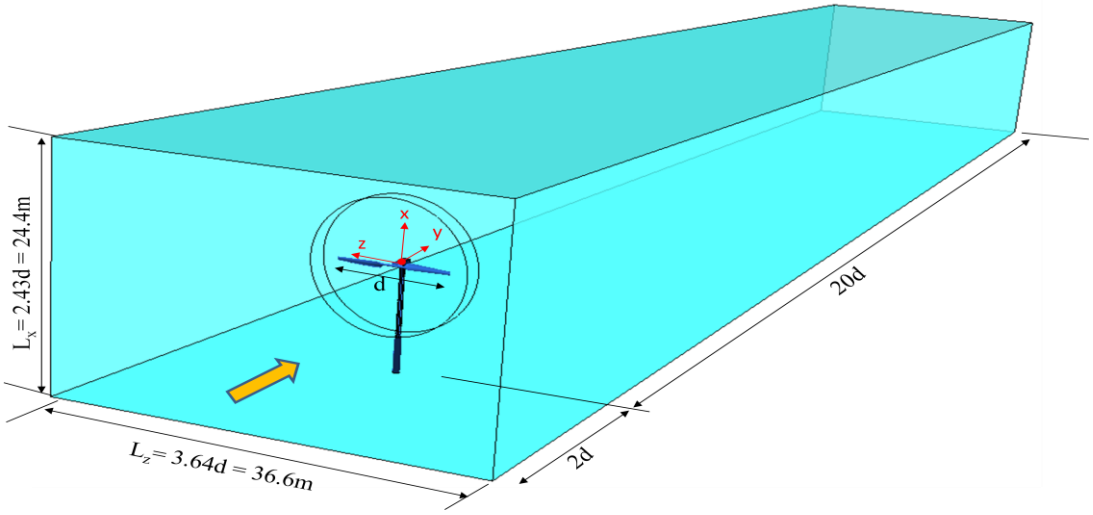

Fig. 2 Schematic diagram of the numerical wind tunnel model with the NREL Phase VI wind turbine. Note that the test section dimensions are the same as that of the NASA Ames 24.4 m × 36.6 m wind tunnel.

The computational domain for the wind turbine placed in the wind tunnel is illustrated in Fig. 3. The domain consists of two parts, the rotationary parts (cylinder and rectangle part) and the stationary part (wind tunnel part). The sliding mesh technique is applied to the moving parts with two mesh interface zones (interface zone 1: cylindrical part and rectangular part, interface zone 2: cylindrical part and wind tunnel part) in the shared faces, where the meshes overlap. The sliding-mesh technique is a recommended method for computation of unsteady flow filed when a time-accurate solution (rather than a time-averaged solution) for rotor-stator interaction is desired. However, it is also the most computationally demanding.

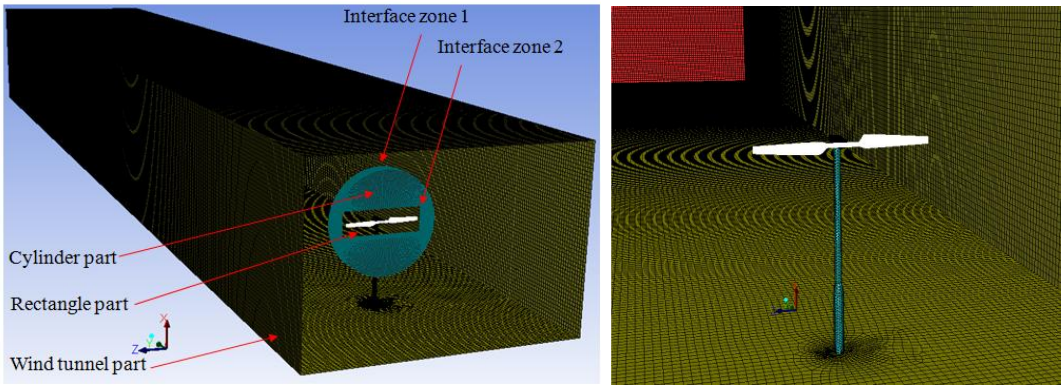

Fig. 3 Computational domain with the rotationary and stationary parts of the mesh.

In order to accurately capture the boundary layer region of the turbine, the rectangle surrounding the blades was composed of hexahedral meshes with 20 inflation layers on the blade surface, a spacing ratio of 1.1 in the normal direction and a first layer of 0.2 mm. The total number of cells in the numerical grid was 3.6 x 10^6, consisting of hexahedral meshes over the entire domain and partially cooper meshes in the cylindrical part. The blade was meshed in the chordwise direction with 100 nodes on both the upper and lower surfaces, with a higher concentration near the leading and the trailing edge regions. Furthermore, 150 nodes were used in the spanwise direction as shown in Fig 4. The blade for the original NREL experiment did not contain a sharp trailing edge. Inclusion of a sharp trailing edge for the simulation also unnecessarily complicates the construction of the hexahedral grids and therefore a blunt trailing edge was used by cutting the blade at 0.99c. It is also important to note that for the downstream wake region, an equal mesh size of 0.25 m interval was used in all directions. This mesh size was the allowable minimum size due to the restrictions defined by the computer resources. Even though grid sensitivity in the wake region affects the wake length and instability, sudden changes in flow patterns were not expected to occur.

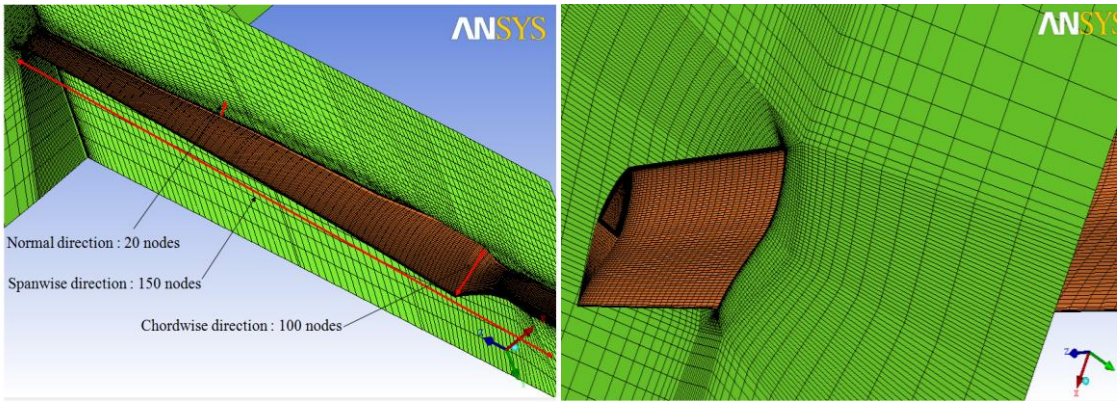

Fig. 4 Grid distribution around the rotor blade.

2.3 Boundary Conditions

Uniform velocity conditions were applied as the boundary conditions for the inlet where the flow enters the computational domain. In order to analyze the effects of wind speed change on the wake instability, upstream wind speeds of 7 m/s, 10 m/s, 13.1 m/s and 15.1 m/s were analyzed while keeping the yaw angle zero. The freestream turbulence intensity was set to 0.2%, regardless of the upstream wind speeds. The upstream or the inlet boundary conditions are the same as the test conditions for the NREL experiments and are summarized in Table 2. For the outlet where the flow leaves the domain, the ambient domain condition (zero pressure) was selected. The spectral synthesizing technique, which is based on the random flow generation technique, originally proposed by Kraichnan (1970) and then modified by Smirnov et al. (2001), was employed for modeling the velocity fluctuations at the inlet. In this method, the fluctuating velocity components are computed by synthesizing a divergence-free velocity-vector field from the summation of the Fourier harmonics.

The present work was carried out using ANSYS FLUENT 13.0, a general-purpose commercial CFD code. FLUENT employs a cell-centered finite-volume method based on a multi-dimensional linear reconstruction scheme, which permits the use of computational elements with arbitrary polyhedral topology, including quadrilateral, hexahedral, triangular, tetrahedral, pyramidal, prismatic, and hybrid meshes. There are several choices for the solver algorithms in FLUENT; including coupled explicit, coupled implicit and segregated solvers. The coupled implicit solver was used in this research exclusively to speed up the convergence. The convective terms were discretised using the Bounded Central Differencing scheme. The courant number was set to 50 and the explicit relaxation factors for momentum and pressure were both set to 0.3. In general, lower values than the default are used to stabilize the convergence behavior in simulations where strong rotating flows are expected. The steady-state computation was first carried out for approximately 1000 iterations to have a convergence below 10^{-3}, and then the unsteady computation used the steady state flow solution as the starting point. The simulation took approximately 120 hours per case on a single CPU with eight cores having processing speed of 2.4 GHz, using the Linux operating system. The blade completed one cycle of revolution in 0.834 s with a time step size of 0.005795 s corresponding to a blade rotation of 2.5 degrees per time-step. LES calculations were performed for sufficiently long flow-times, of the order corresponding to 30 revolutions of the turbine blades, to obtain stable statistics of the flow and turbulence. In order to calculate the root-mean-squares of all the variables, such as velocities in x, y and z directions, pressure and turbulence intensities, 1440 data samples were taken, over the last ten rotations of the wind turbine blades.

Table 2. Boundary conditions at the inlet.

	Wind speed (m/s)	RPM	ρ (kg/m^3)	TI (%)
Case1	7	71.9	1.246	0.2
Case2	10	72.1	1.246	0.2
Case3	13.1	72.1	1.227	0.2
Case4	15.1	72.1	1.224	0.2

2.4 Large eddy simulation based on dynamic Smagorinsky-Lilly model

In order to overcome the limitations of unsteady RANS, such as being incapable of capturing unsteadiness arising from vortex shedding, LES was performed, based on the dynamic Smagorinsky-Lilly model. However, it is important to note that the LES requires much larger simulation times as compared to the unsteady RANS. The governing equations in LES are obtained by filtering the original Navier-Stokes equations. The filtered continuum and Navier-Stokes equations are given as follows:

$$\frac{\partial \rho}{\partial t} + \frac{\partial}{\partial x_i}(\rho \bar{u}_i) = 0 \quad (1)$$

$$\frac{\partial}{\partial t}(\rho \bar{u}_i) + \frac{\partial}{\partial x_j}(\rho \bar{u}_i \bar{u}_j) = \frac{\partial}{\partial x_j}(\sigma_{i,j}) - \frac{\partial \bar{p}}{\partial x_i} - \frac{\partial \tau_{i,j}}{\partial x_j} \quad (2)$$

Here $\bar{u}_i$ is the resolved velocity in i-direction (i=1, 2, and 3 correspond to the x, y and z directions), $\sigma_{i,j}$ is the stress tensor due to molecular viscosity and $\tau_{i,j}$ is the subgrid-scale stress. These are defined by the following equations:

$$\sigma_{i,j} \equiv \left[\mu\left(\frac{\partial \bar{u}_i}{\partial x_j} + \frac{\partial \bar{u}_j}{\partial x_i}\right)\right] - \frac{2}{3}\mu \frac{\partial \bar{u}_l}{\partial x_l}\delta_{i,j} \quad (3)$$

$$\tau_{i,j} \equiv \rho\,\overline{u_i u_j} - \rho\,\bar{u}_i \bar{u}_j \quad (4)$$

The subgrid-scale stresses resulting from the filtering operation are unknown, and require modelling. The subgrid-scale turbulence models employ the Boussinesq hypothesis (Hinze, 1975) as used in the RANS models and therefore the subgrid-scale turbulent stresses can be computed from the following:

$$\tau_{i,j} - \frac{1}{3}\tau_{k,k}\,\delta_{i,j} = -2\,\mu_t\,\overline{S_{i,j}} \quad (5)$$

Here μ_t is the subgrid-scale turbulent viscosity. The isotropic part of the subgrid-scale stresses $\tau_{k,k}$ is not modelled, but is added to the filtered static pressure term. The rate of strain tensor for the resolved scale is represented by $\overline{S_{i,j}}$ and is defined by the following expression:

$$\overline{S_{i,j}} \equiv \frac{1}{2}\left(\frac{\partial \bar{u}_i}{\partial x_j} + \frac{\partial \bar{u}_j}{\partial x_i}\right)$$

This simple model was first proposed by Smagorinsky (1963). In the Smagorinsky-Lilly model, the eddy-viscosity is modelled by

$$\mu_t = \rho\,L_S^2|\bar{S}| \quad (6)$$

where L_S is the mixing length for subgrid scales and is computed using $|\bar{S}| \equiv \sqrt{2\,\overline{S_{i,j}}\,\overline{S_{i,j}}}$, and

$$L_S = \min\,(\kappa d, C_S\,V^{1/3}) \quad (7)$$

Here κ is the von Karman constant, d is the distance to the closest wall, C_S is the Smagorinsky constant, and V is the volume of the computational cell. Lilly (1992) derived a value of 0.17 for C_S for homogeneous isotropic turbulence in the inertial subrange. However, this value was found to cause excessive damping of large-scale fluctuations in the presence of mean shear and in transitional flows near solid boundaries, and had to be reduced in such regions. In short, C_S is not a universal constant, which is the most serious shortcoming of this simple model. Germano et al. (1991) and subsequently Lilly (1992) conceived a procedure in which the Smagorinsky model constant, C_S is dynamically computed based on the information provided by the resolved scales of motion. The dynamic procedure thus obviates the need to specify the model constant C_S in advance. Further details for the validation of this model can be found in the work of Kim (2004). The C_S obtained using the dynamic Smagorinsky-Lilly model varies in time and space over a fairly wide range. In ANSYS FLUENT, C_S is also clipped at zero and 0.23 by default. In this study, the dynamic Smagorinsky-Lilly model was applied to yield the best results for a wide range of flows.

3. Results and discussions

3.1 Validation of the simulation

3.1.1 Comparison of pressure coefficients

It is very important to compare the results of LES with the experimental data since the wake characteristics of a wind turbine are closely related to the changes in the axial and angular momentum (Burton, 2001) that cause the pressure distribution on the blade. Accurate predictions of the pressure coefficients along the blade therefore provide the necessary validation for the subsequent wake analysis. The measured and computed pressure distributions at different spanwise locations along the blade length for wind speeds of 7 m/s and 10 m/s at

yaw angle of 0^O are shown in Fig. 5. The spanwise sections presented are at normalized distances of r/R = 0.3, 0.63 and 0.95, as shown in Fig. 5 (a). The computed LES results show a very good quantitative agreement with the pressure measurements from the experiment (Hand et al., 2001 ; Simms et al., 2001) for all the sections along the blade length, as shown in Fig. 5 (b) and (c). Small discrepancies, however, do exist near the suction side at x/c = 0 for r/R = 0.95 in the outermost region of the blade when the upstream wind speed is 7 m/s (Fig. 5 (b - iii)). These discrepancies might be due to the tip vortices and the radial flows from the root moving towards the tip, caused by centrifugal acceleration (Mo and Lee, 2012). Similarly, discrepancies can be observed at the other stations for an upstream wind speed of 10 m/s (Fig. 5 (c - i, ii)). This can also be attributed to the radial flows induced by centrifugal acceleration, however, for the airspeed of 10 m/s, the blade is primarily undergoing stall due to large angles of attack. This might be a plausible cause of the slight inconsistency observed at the inboard regions. On the other hand, the close proximity of these regions to the complicated hub geometry might also induce some differences in the measured and calculated pressures. This is primarily because the simulated hub assembly is far less intrusive as compared to the heavily instrumented hub used in the experiment. Nonetheless, these discrepancies are of such small magnitudes that they are unlikely to affect the flow field in the wake of the turbine. Therefore, the subsequent wake analysis presented is considered to be of sufficient accuracy.

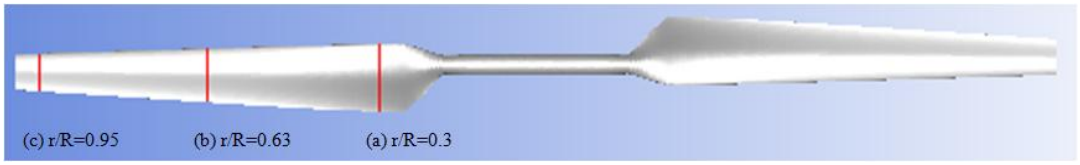

(a) Selected spanwise segments along the blade length.

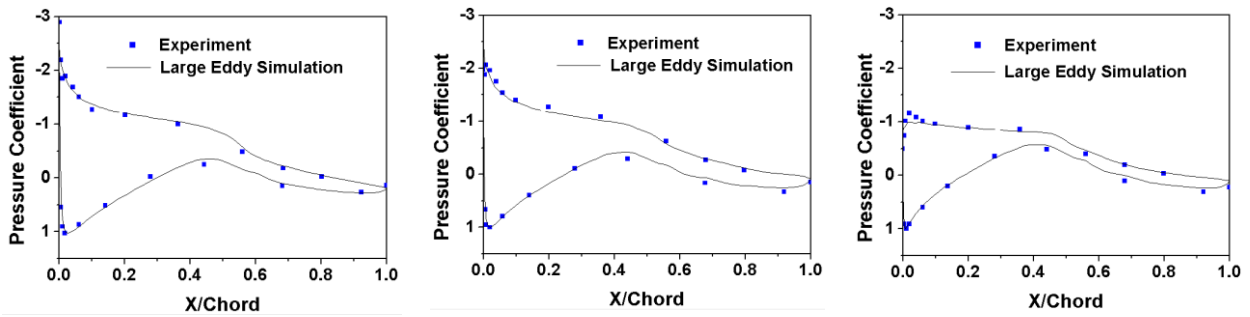

(i) r/R=0.3 (ii) r/R=0.63 (iii) r/R=0.95

(b) Wind speed of 7m/s

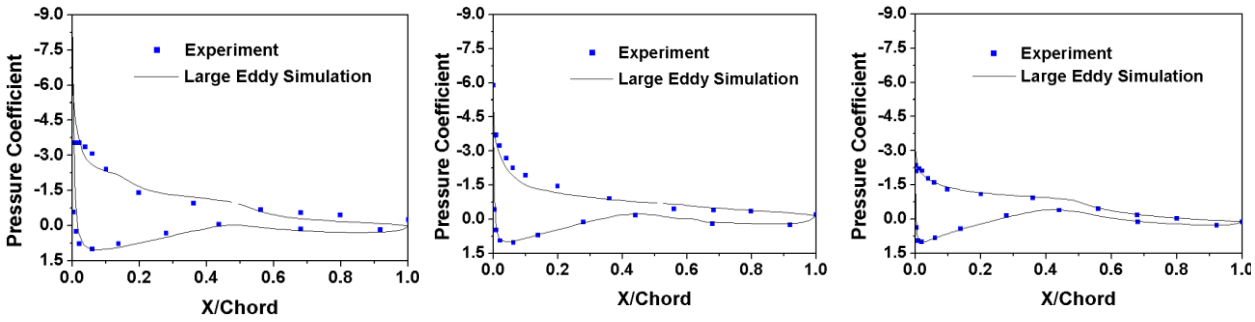

(i) r/R=0.3 (ii) r/R=0.63 (iii) r/R=0.95

(c) Wind speed of 10m/s.

Fig. 5 Comparisons of the chordwise time-averaged pressure coefficient obtained from the experiment (Hand et al., 2001; Simms et al., 2001) and the LES at selected spanwise sections (a) along the blade at inlet velocities of 7 m/s (b) and 10 m/s (c).

3.1.2 Comparison of power outputs

The fluctuations of the power outputs of the wind turbine under different wind speeds are shown in Fig 6. The power curve for 7 m/s shows a relatively stable behaviour with time, whereas the power curves for 10 m/s, 13.1 m/s and 15.1 m/s show highly fluctuating characteristics,

as observed in Fig. 6 (a). These power fluctuations are mainly caused due to the separation of the flow near the outboard regions of the blades at the higher airspeeds as observed in the original experiment performed by the NREL (Hand et al., 2001; Simms et al., 2001). This statement can be further investigated using the unsteady LES performed in the current article through the extraction and analysis of the time dependent pressure distributions. However, it is believed that such an endeavour would deviate from the scope of the present article and, therefore, was not pursued.

The fluctuating power curve has spectral attributes and it is often useful to analyze them for interpretation of the time-sequence data from a transient solution. In signal processing, the Fast Fourier Transform (FFT) enables us to take any time-dependent data and resolve it into an equivalent summation of sine and cosine waves. In the current research, FFT analysis using 1440 sampling power data acquired at each time step was performed and the results are presented in Fig 6 (b). The figure indicates the most prevalent frequency components of the oscillating power curves along with their respective amplitudes. For clarity, the first frequency component and the corresponding amplitude of the fluctuating power curves are presented in Fig. 6(c) as a function of the freestream wind speed. It is interesting to note that as the wind speed increases, an increase in first frequency component is observed till the wind speed reaches 13.1 m/s. Afterwards, a decrease in the first frequency is observed, indicating that the frequency component of the fluctuating power curve tends to spread out. However, the amplitude of oscillation is observed to increase as the wind speed increases. This is primarily due to the occurrence of stall on the turbine blades. The amplitude characteristics, calculated using the FFT analysis, are therefore representative of the fatigue loads on the wind turbine.

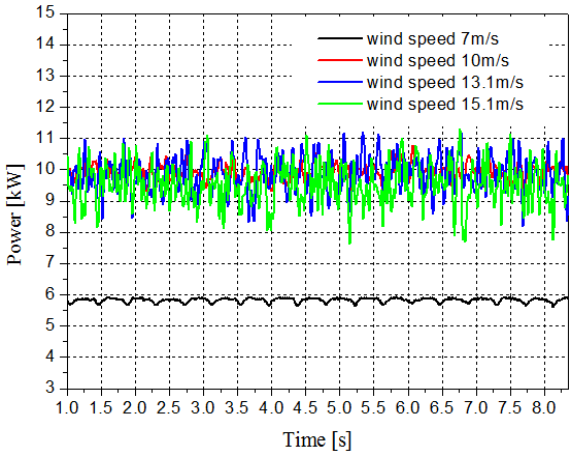

(a) Fluctuating output power for different wind speeds.

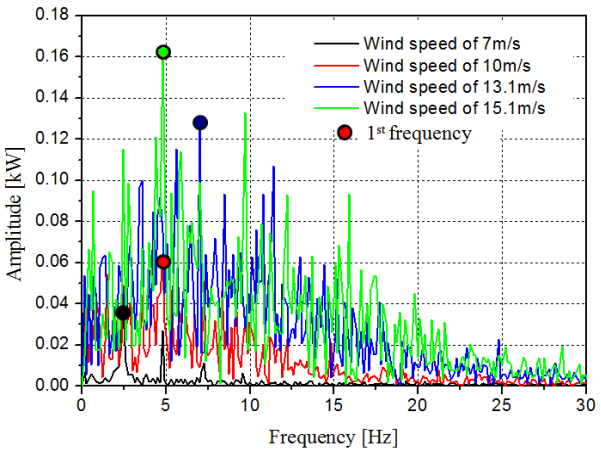

(b) FFT analysis using 1440 sampling data of power for each wind speed.

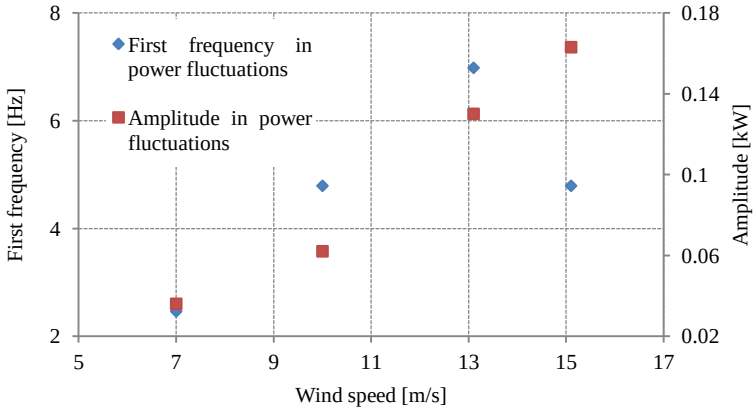

(c) Variation of the 1st frequency and the amplitude in power fluctuations as a function of airspeed

Fig. 6 Output power characteristics for different wind speeds from the simulation.

The time-averaged power for wind speeds of 7 m/s, 10 m/s, 13.1 m/s and 15.1 m/s are 5.83 kW, 9.93 kW, 9.9 kW and 9.5 kW, respectively as shown in Fig. 7. The average power starts to increase from the lower wind speed of 7m/s and reaches its maximum value at a wind speed

of 10m/s. However, at higher wind speeds, the time-averaged power starts to plateau and then decrease. The decrease in the power is due to the NREL Phase VI wind turbine being stall-regulated. The wind turbine was designed so that the blades will stall after a specific wind speed, without the requirement of any pitch control. Therefore, the operating state of the turbine can be categorized into two states: pre-stall and post-stall. The flow and TI characteristics are dependent on these states, as discussed later in the article.

As presented in Table 3, LES calculations in the present study show a very good agreement with the measured power outputs. A slight under-prediction of 3.1% is observed at the lower wind speed of 7 m/s whereas an over-prediction of 6.6% is observed at the highest wind speed of 15.1 m/s. For the intermediate wind speeds, the percentage error in the power output is even smaller. It is believed that this difference in the power outputs comes from two major factors. The first is the convergence criteria for the residuals in calculations of LES. Convergence criteria sensitivity analysis was performed for two values of 1×10^{-3} and 2×10^{-3}. It was found that the average power with 1×10^{-3} criterion showed a 2% better result than the 2×10^{-3} criterion, for one cycle of revolution of the wind turbine blade at a wind speed of 7 m/s. However, the computational time associated with the 1×10^{-3} criterion was approximately twice as much when compared with 2×10^{-3} criterion, due to the lower slope of the residual curve. Therefore, the convergence criterion for the residuals was set to 2×10^{-3}. The second reason might be the grid density in the computational analysis, but due to limited computer resources, no grid sensitivity checks could be performed at this stage. However, it can be anticipated that the grid sensitivity will have a little effect on the power output in the pre-stall state, primarily due to the use of good quality mesh for the boundary layer regions of the blade surface. However, a much larger mesh density is required to accurately capture the complex flow generated at high angles of attack in the post-stall state. This is the reason that a slightly larger error in the output power is observed in the post-stall state at the larger wind speed. Despite the limitations imposed by the computer resources, it can be observed that the LES results are still more accurate than those produced by previous researches, where steady-state calculations with two-equation turbulence models were used. The results from these researches are also summarized in Table 2 where it can be noted that the power output errors range from a minimum of 4.4% up to a maximum of 23.6% when compared with the experimental data (Hand et al., 2001 ; Simms et al., 2001).

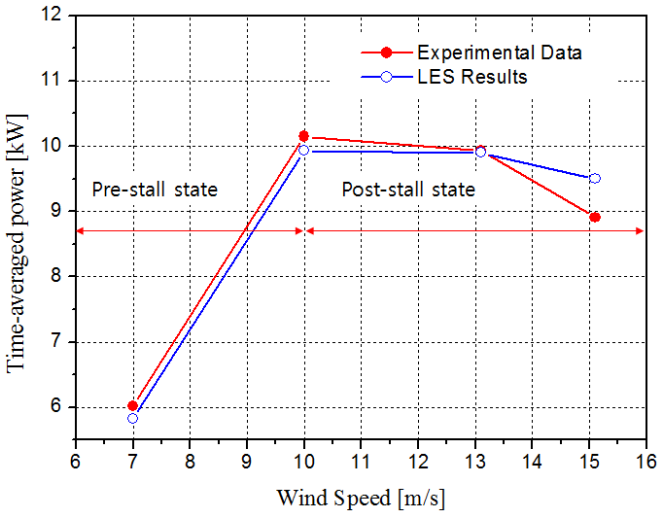

Fig. 7 Comparison of the time-averaged power at different wind speeds obtained using LES with the experimental results.

Table 3. Comparisons of power outputs at different wind speeds from different studies with the experimental results.

Inlet Condition	Power [kW]				Percentage Error in Power			
Wind Speed (m/s)	7	10	13.1	15.1	7	10	13.1	15.1
Experiments (Hand et al., 2001 ; Simms et al., 2001)	6.01	10.15	9.93	8.91	-	-	-	-
Sørensen et al. (2002) (free condition)	5.45	12.15	9.49	6.80	9.32	19.46	4.46	23.64
Menter et al. (2006)	7.03	9.27	8.57	8.05	16.98	8.71	13.71	9.61
LES (Present study)	5.83	9.93	9.9	9.5	3.09	2.17	0.30	6.62

The turbulent wake measurements of the NREL phase VI wind turbine performed in the NASA Ames wind tunnel were restricted to mean velocity measurements in the immediate wake of the turbine operating at a yaw angle of 60 deg (Hand et al., 2001). The purpose of these

measurements was to study wind turbine furling. For the present case, however, these measurements could not be used for the purpose of validation since the simulations in the current work have been performed at a yaw angle of zero degrees. However, since aerodynamic characteristics like the pressure coefficients and power output have been predicted with reasonable accuracy, and since the turbulent wake characteristics depend largely on these aerodynamic parameters, such as the leading and trailing edge separation (Corten and Nederland, 2001), the turbulent wake analysis that follows is considered to be sufficiently accurate. Moreover, since LES is a suitable tool for transition prediction, resolving a wide range of length and time scales (Launder and Sandham, 2002), therefore, it is expected that applying it will lead to useful conclusions.

3.2 Velocity profiles in the wake

Before presenting the velocity profiles in the wake of the turbine, it is important to first consider the variation of angle of attack along the turbine blades as a function of wind speed. Such an analysis will assist in deciphering the primary trends of wake velocity behaviour and will indicate the ability of the wind turbine to extract useful momentum from the oncoming flow. The distribution is presented in Fig. 8. The angle of attack referring to a relative flow velocity can be calculated using an inflow wind speed and a global pitch angle relative to the plane of rotation. For the wind speed of 7m/s, in the pre-stall state, it can be observed that the angle of attack along the blade length is smaller than the 2D stall angle of 16° for the S809 airfoil (Hand et al., 2001). Therefore, the flow is expected to be fully attached along the entire span of the blade. It can also be observed that the angle of attack along the blade length is varying. The reason for this variation is due to the rotation of the turbine blades; the inboard regions, rotating at smaller tangential velocities, show much larger angles due to the increasing wind speed component as compared to the outboard regions. For the wind speed of 10m/s, the angles of attack along most of the blade are greater than 16°, except for the tip region (r/R>0.85). This might be considered as a transitional phase for the flow since part of the blade has experienced flow separation. As the wind speed is further increased, the angle of attack along the entire blade length becomes greater than 16°, indicating that the wind turbine is now operating in the complete post-stall state.

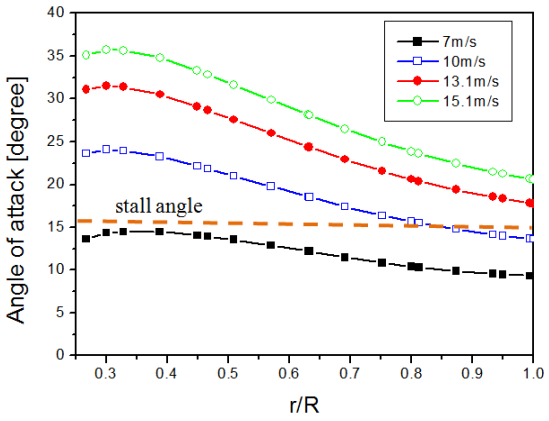

Fig. 8 Angle of attack variation along the rotor blade from the hub to tip for various wind speeds.

The vertical profiles of the time-averaged normalized axial velocities for one upstream and several normalized downstream locations behind the turbine for -1.14 <x/d< 1.28 and at the hub centre (z/d = 0) are presented in Fig. 9. The results here show the velocity deficit due to momentum extraction of the wind turbine and the consequent recovery behind the wind turbine in the wind tunnel model. The axial velocities (V_y) have been normalized with the corresponding reference wind speeds and therefore the normalized velocities at the upstream station are 1. As it can be seen in Fig 8, a near-symmetrical behaviour of the velocity profiles can be observed about the hub centre for the region of -0.5 <x/d <0.5 corresponding to the rotor blade. However, an asymmetrical velocity profile is observed when the effects of the tower are included.

At the upstream location of y/d= -1, it can be observed that the normalized velocity is the same, except for region of -0.5 <x/d <0.5, where the velocity is approximately 0.08% lower than the reference wind speed for all the cases. This is due to the stagnation effect and the consequent expansion of the stream-tube of air approaching the wind turbine. Similarly, the boundary layer on the tunnel walls is also apparent at the upstream station. Right after the airflow passes through the wind turbine, there is a clear evidence of the turbine extracting momentum from the incoming uniform flow and hence producing a wake. This can be observed from the regions of reduced velocity, or velocity deficit zones, at y/d=1 where the W-shaped velocity profiles are apparent. It can be observed that for the regions corresponding to the turbine blades, the maximum momentum extraction and hence the normalized velocities are a function of the upstream reference

velocity. The largest velocity reductions are observed for the case of the smallest upstream tunnel speed of 7 m/s. However it is important to note that largest velocity reductions do not imply more power generation, since the power output is a function of the cube of the upstream velocities. The largest velocity deficit might be due to the state of the flow on the turbine blade; since at 7m/s, the flow is completely attached to the entire blade surface and therefore a larger proportion of energy is extracted from the upcoming flow.

The additional momentum deficit due to the presence of the tower is also apparent from the velocity profiles presented in Fig. 9, where a larger velocity reduction is observed as compared to the upper portion of the tunnel. As the upstream wind speed increases, the corresponding velocity deficits downstream of the turbine disc become less pronounced, while retaining similar profile shapes. These profile shapes can largely be attributed to the aerodynamic design of the blades and the rotor hub. In particular, the variation of angle of attack on the turbine blade plays a very important role in determining the wake characteristics behind a wind turbine, because it is closely related to the change of axial and angular momentum of a wind turbine (Burton, 2001).

There exists considerable difficulty in defining the wake width from the present numerical results, due to the flow being constrained by the wind tunnel and due to the interference caused by the tower. Therefore, the wake width needs to be explained qualitatively, rather than suggesting a quantitative relationship between the wake width and downstream distance for different wind speeds. In future research, quantitative estimation will be conducted by simulating a wind turbine in the open environment. In the current research, the wake width is defined using the wind speed ratio, as the region where the wind speed ratio is smaller than 0.99. Using this definition of the wake width, it is interesting that the wake width is independent of the upstream wind speed and remains approximately constant up to $y/d = 2$, and afterwards expands linearly for distances as large as 20 rotor diameters in the far-wake. This causes the normalized velocities to exceed one at large downstream distances for almost all the regions, except for the regions in the centre corresponding to the wind turbine hub.

At $y/d = 1$ and $y/d = 2$, the peaks of the W-shaped profiles with the lowest velocity deficits are found in the zone of $-0.1 < x/d < 0.1$, corresponding to the inboard regions of the wind turbine. It can be observed that the velocity deficits in this zone become larger until $y/d = 6$ beyond which the opposite behaviour is observed. This continues until the W-shaped velocity profiles become V-Shaped velocity profiles at $y/d = 8$. After this station, the velocity deficits in the wake decrease to $y/d = 20$. This is apparently because the turbulence in the wake acts to redistribute the momentum from outside the wake into the centre of the wake. In this way, momentum is transferred into the wake, the wake expands, and the velocity deficit is reduced. However, the wake effects still remain noticeable even in the far-wake at distances as large as 20 rotor diameters. It is also worth noting that the velocity profile near the walls of the tunnel are slightly developed at $y/d= -1$, prior to the wind turbine. The velocity deficit near the wall increases as the downstream distance is increased and reaches approximately 0.7 at $y/d = 20$ due to boundary layer effect. Due to the continuous development of the wall boundary layer, the normalized velocities for region of $0.75 < x/d < 1$ exceed the value of 1, indicating larger velocities than the upstream wind speeds.

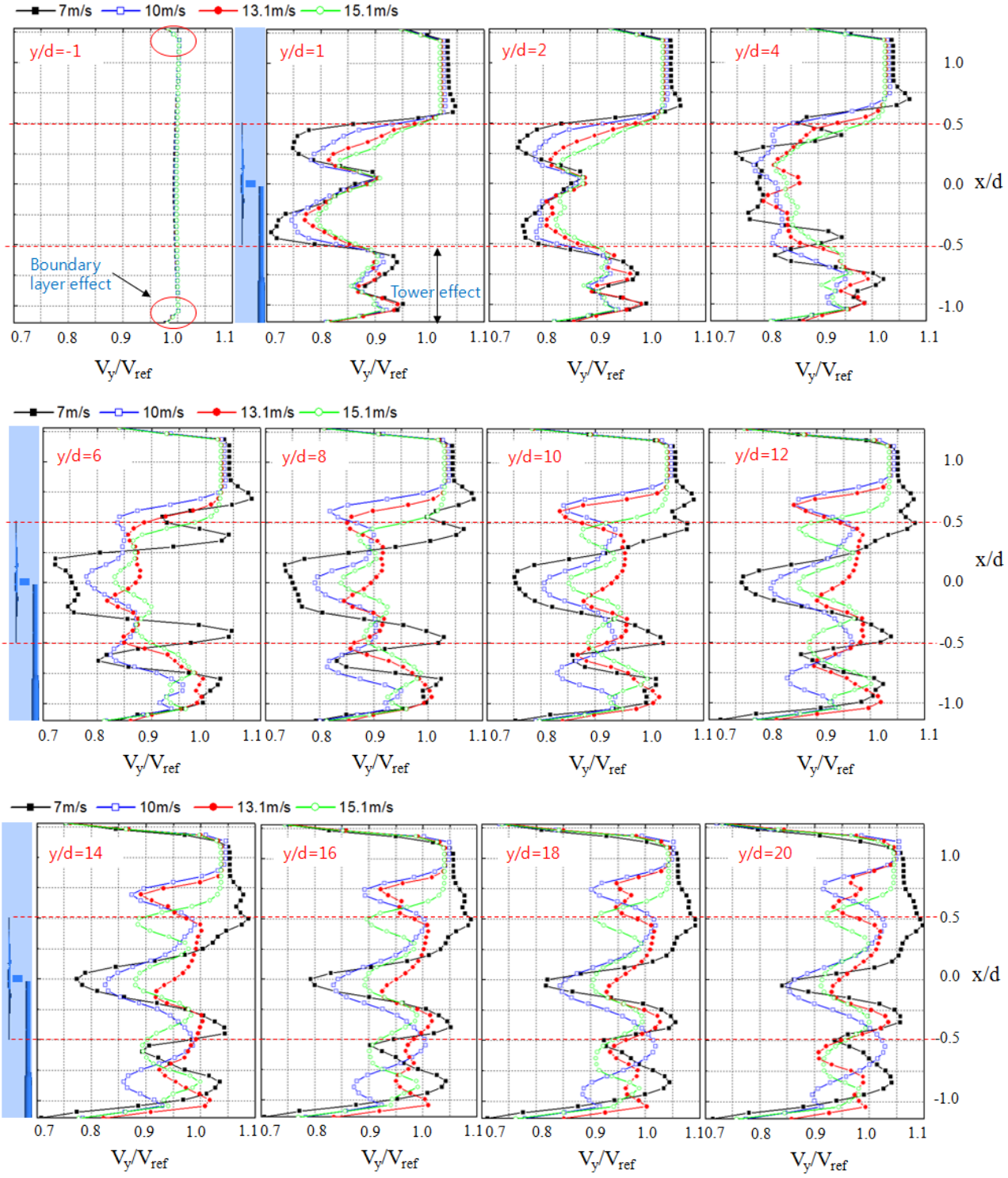

Fig. 9 Comparison of vertical profiles of the time-averaged normalized y-velocity for one upstream and eleven downstream locations for -1.14 <x/d< 1.28 and at the hub centre (z/d=0).

The discrete annular segments used to extract the mean axial velocity through the rotor plane are illustrated in Fig. 10. The choice of the annular segments indicated in the figure is arbitrary and is to illustrate general trends during the process of energy extraction. The innermost annular segment corresponds to the blade root where the blade meets the elliptical connecting shaft, whereas the outermost segment corresponds to the blade tip. Comparison of the normalized y-velocities for selected downstream locations with different upstream wind speeds behind the selected annular segments is presented in Fig. 11. It can be seen that the largest difference in the mean axial velocities, for

all cases and all annular segments, exist just downstream of the wind turbine. This indicates that a fluid element passing through the rotor disc looses part of its kinetic energy due to the energy extraction from the wind turbine. However, the process of energy extraction varies, depending upon whether the wind turbine is operating in the pre-stall or the post-stall state. Furthermore, it is observed that each part of the turbine blade (each annular segment) plays a varying role during the process of energy extraction.

For the NREL Phase VI wind turbine, the upstream wind speed of 10 m/s divides the two operating states of pre- and post-stall. Therefore, in this research, the condition corresponding to the pre-stall state is when the upstream wind speed is 7 m/s, based on Fig. 7 and 8. Note that among the five selected spanwise sections, smaller reductions in the axial velocities for the two sections of r/R=0.267 and 1, corresponding to the root and tip, are observed at wind speed of 7 m/s than at the other three sections of r/R=0.5, 0.75 and 0.9, even though the angle of attack along the entire blade length is smaller than the stall angle. The NREL Phase VI rotor blades were designed to be thicker at the root, where the maximum thickness-to-chord ratio is 47% at r/R=0.2 in comparison to the average 21% along the length of the blade. The elliptic shape at the root causes the flow to pass through the rotor disc at a lower angle of attack with minimum energy extraction. In addition, near the tip, the tip vortices occur due to the local cross flow along the trailing edge and result in an uneven pressure distribution. This uneven pressure distribution sequentially causes the approaching flow towards each blade element to change its path (Mo and Lee, 2012). For these reasons, the reductions in axial velocity at the root and the tip are lower as compared to the other three locations.

When the wind speed is 10m/s, which is the transitional phase as mentioned in regards to Fig. 8, the reduction in axial velocities at the root (r/R= 0.267) start to increase due to the angle of attack being larger than the stall angle. For wind speeds more than 10m/s, the reduction in axial velocity at r/R= 0.5 is the largest as compared to the other regions. This is due to the fact that the flow has separated from the blade and the blade now acts more like a flat plate. The larger angle at the root therefore causes a larger separation zone and larger velocity deficit as compared to the other regions. Downstream of y/d = 1, for all wind speeds, velocity recovery starts to increase the axial velocities in the wake. The main reason for different velocity recoveries at different sections is due to the difference of the flow patterns after the vortex breakdown. These flow structures in the wake are closely related to the velocity recovery in the wake and are explained in detail in Section 3.3. Comparisons of the time-averaged y-velocity contours with different flow structures downstream of the wind turbine for different upstream wind speeds are shown in Fig. 12. It is observed that the flow structures in the wake show different patterns according to wind speeds. Additionally, the effects of the tower shadow can be observed by the relatively reduced velocities in the wake of the tower. Through this visualization, it can be inferred easily that the velocity recovery and the flow structures in the wake are closely related.

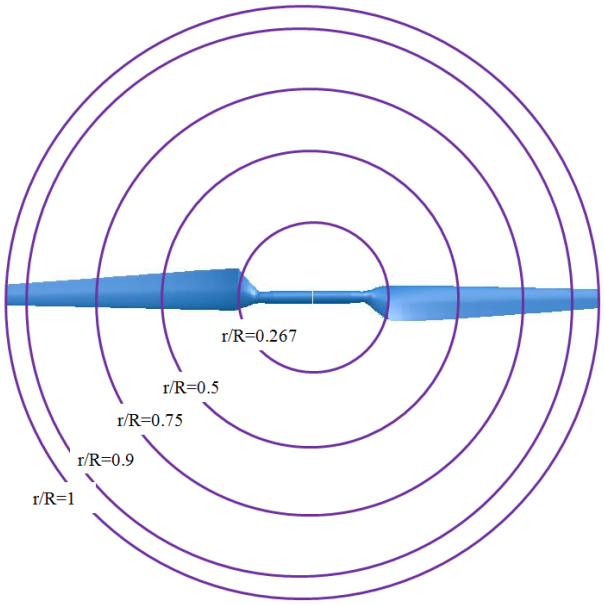

Fig. 10 Discrete annular segments used to extract the mean axial velocity through the rotor plane.

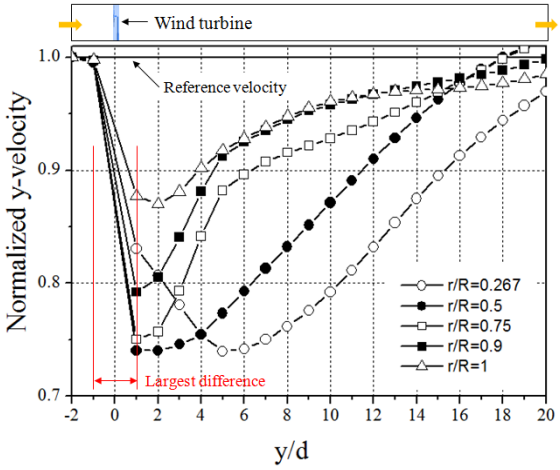

(a) Wind speed of 7m/s.

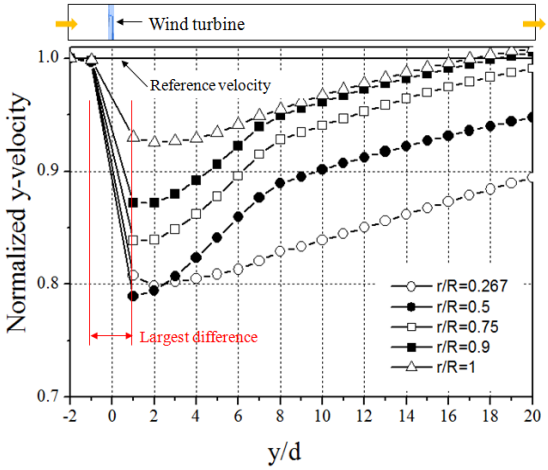

(b) Wind speed of 10m/s.

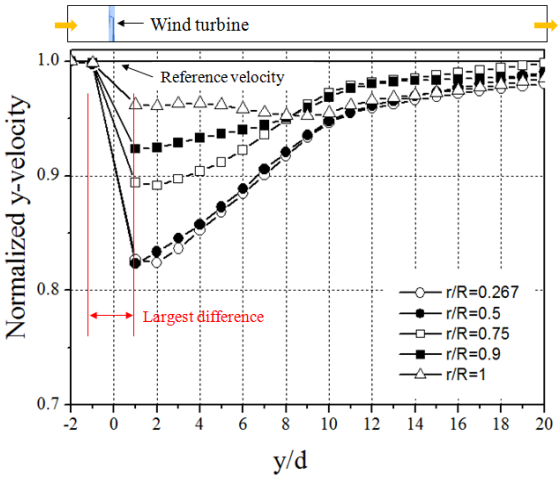

(c) Wind speed of 13.1m/s.

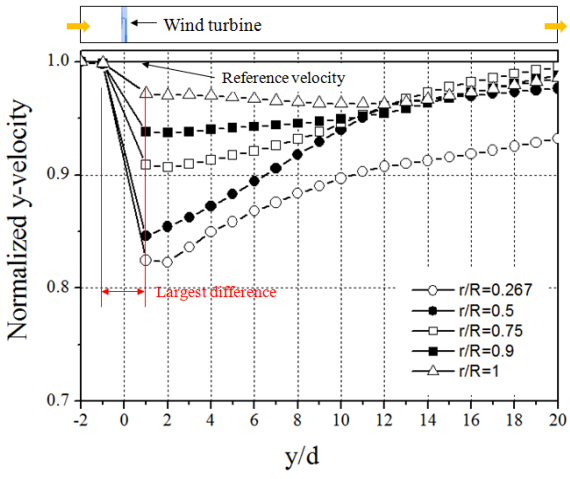

(d) Wind speed of 15.1m/s.

Fig. 11 Comparison of normalized axial velocity for selected downstream locations for different wind speeds.

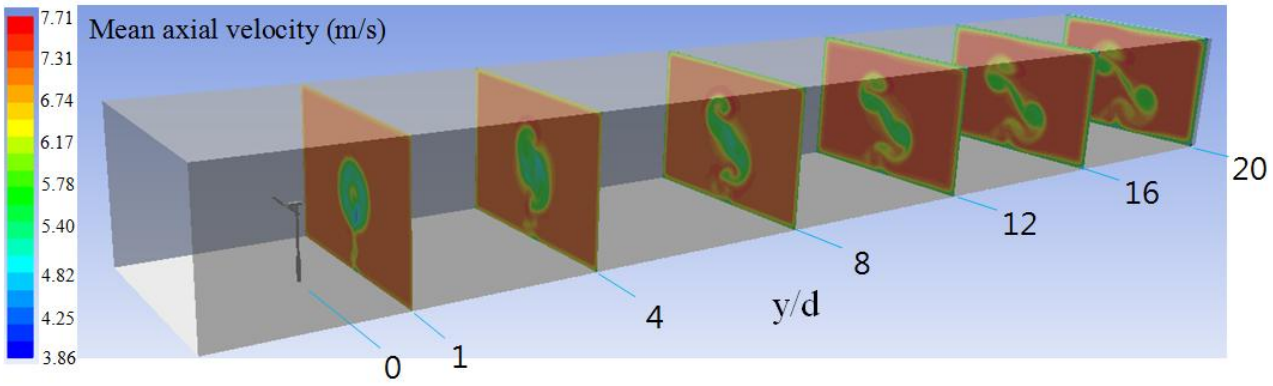

(a) Wind speed of 7m/s.

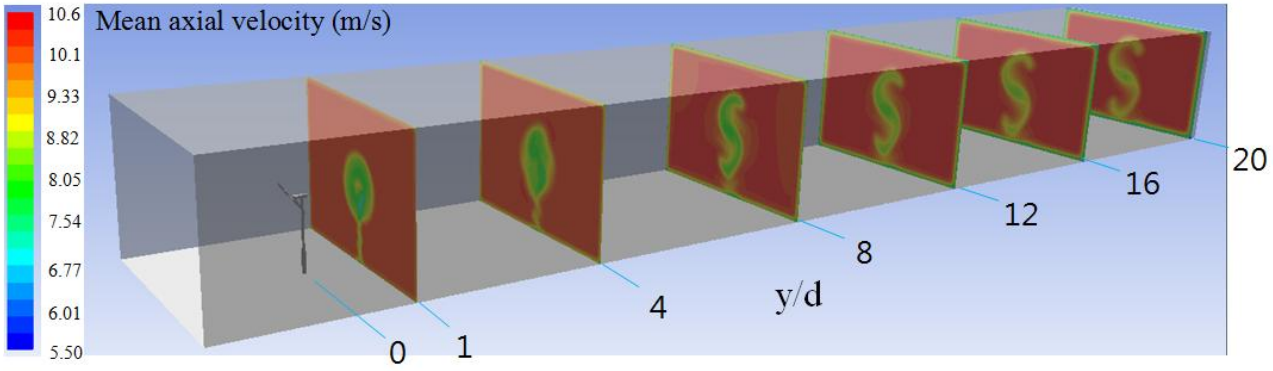

(b) Wind speed of 10m/s.

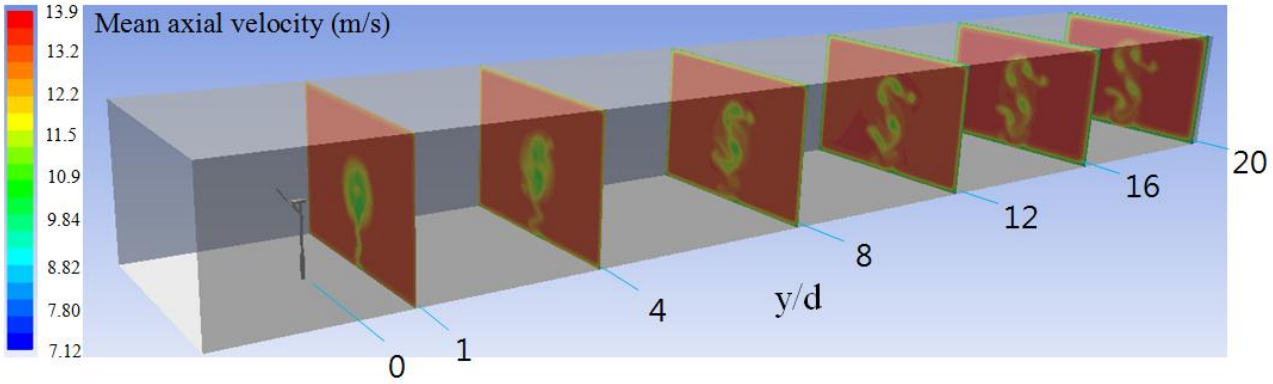

(c) Wind speed of 13.1m/s.

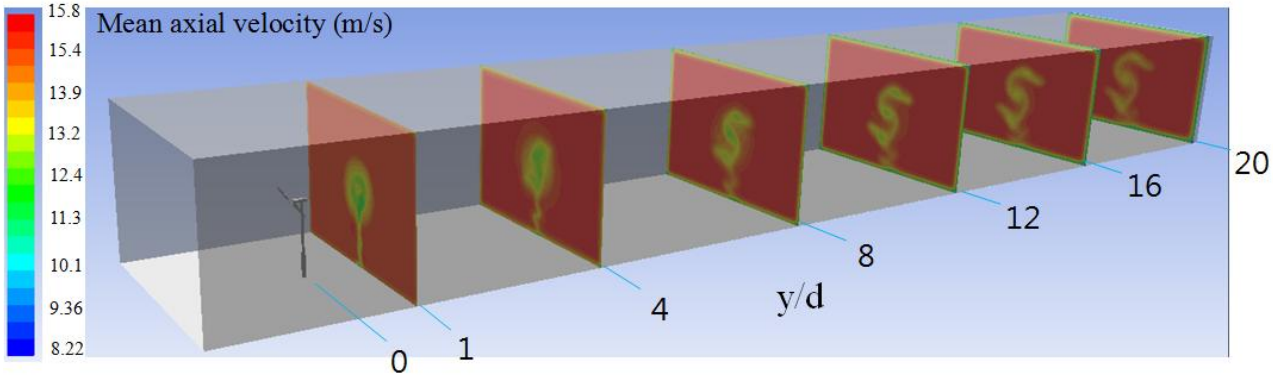

(d) Wind speed of 15.1m/s.

Fig. 12 Comparison of time-averaged y-velocity contours at each section.

3.3 Flow structures and wake instability

The flow structures behind a three bladed wind turbine are illustrated in Fig. 13, showing the strong tip vortices, located at the edge of the rotor wake, the central helical vortex structure from the root, which lies along the axis of the rotor, and the bound lift-generating vortices in the blade (Hansen, 2008). Among these vortices, the tip and root vortices have been studied in different investigations over the last few decades; however, the root structure is not generally considered to be as important as the tip vortex structures. This is because the root vortices from each blade are much closer to each other as compared to the tip vortices and the helical structure is therefore destroyed earlier. The stability of the tip vortex thus dictates the basic dynamic behaviour of the far-wake (Ivanell et al., 2007). The purpose of presenting the illustration in Fig. 13 is to highlight some of the key flow features that are expected to occur in the wake, as observed by previous researchers and in order to facilitate correlation with the current simulation.

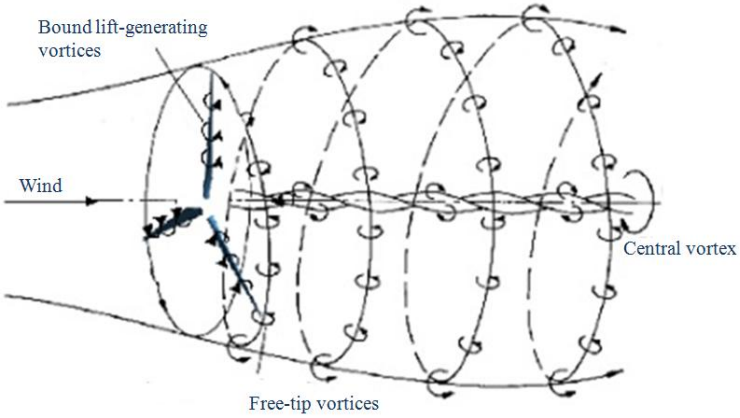

Fig. 13 Sketch of the vortex system behind a wind turbine (Ivanell et al., 2007).

Fig. 14 depicts the instantaneous y-component of vorticity at the selected axial locations for different wind speeds. It is important to note that the contours presented might not be of sufficient resolution due to the coarse mesh used in the wake. However, for the purpose of the current work the mesh density and resolution were sufficient to establish the global trends in the flow field such as evolution and breakdown of the vortical structures and correlations with turbulence intensities. Therefore, in order to avoid much larger simulation times, a finer mesh was not used. It is also worth stating that simulations were conducted at coarser meshes during the initial setup and it was confirmed that the solution was approaching mesh-independence as the mesh density was sequentially increased. The slight discrepancies that might have occurred due to the coarse mesh have been highlighted in the discussions that follow.

In Fig. 14, it can be observed that immediately downstream of the wind turbine, the wake is a system of intense and coherent rotating helical vortices. Several important vortex structures can be identified in the contour plots, including the ring of high vorticity being generated by the rotating tips of the blades, and the streamwise vortex generated by the hub and the tower vortices. Note that the effects of the coarser mesh are clearly visible since the tip vortices are slightly distorted. Furthermore, the blade root vortices appear as a single streamwise vortex instead of a tightly wound helical vortex structure. This is also due to the resolution constraints posed by the current mesh. Nonetheless, it is interesting to note that the tightly wound vortices in the wake become unstable, depending on the freestream wind speed, as the flow progresses downstream and finally collapse. The collapse occurs due to the mutual interaction of the vortex structures in the near wake and the influence of the wall bounded flow outside the wake. The growth of the boundary layer at the tunnel wall as the flow progresses downstream, observable in Fig. 9, significantly alters the wake flow and results in, what has been termed in the article as, wake instability. After the initial breakdown of the spiral vortices, it can be observed that flow very quickly organizes itself into stream wise counter-rotating vortex pairs, even during operation in post-stall regimes. The phenomenon of vortex breakdown can also be observed in the field experiment tests performed at the Risø test centre in Denmark (Web reference: [2]) and the NASA Ames 24.4 m × 36.6 m wind tunnel test by the NREL (Web reference: [1]), as shown in Fig. 15. In the field experiment, a single blade turbine was investigated to avoid disturbances from the other blades and the tip spiral was identified by smoke exiting the blade at two radial positions close to the tip. As can be observed, the tip spiral becomes unstable at approximately 3 rotor radii (1.5d) downstream of the turbine in case of the Risø test whereas in the wind tunnel experiment, as shown in Fig. 15(b), it becomes unstable at a much larger downstream location. The clear diffusion of the ring vortex originating from the tip of the blade in Fig 15 (b) is indicative of vortex breakdown and the near-wake collapse. The earlier breakdown during the field experiment could be explained by the presence of higher atmospheric turbulence, rapidly changing direction of the oncoming wind vector, interference due to a complicated tower, uneven ground effects, the momentum exchange between surrounding air and the wake, and the velocity gradients in the atmospheric boundary layer.

From Fig. 14, it can be observed that the vortex structures in the wake transition to a sinuous shape at y/d = 4, 6, 9 and 11. Then, due to wake instability, these unstable structures completely breakdown at y/d = 6, 8, 11, 13 for wind speeds of 7 m/s, 10 m/s, 13.1 m/s and 15.1 m/s respectively. For an upstream wind speed of 7 m/s (Fig. 14 (a)), it can be observed that as the normalized downstream distance increases, the collapsed spiral wake spreads and after y/d = 6 results in the formation of two counter-rotating vortex pairs. The pair of counter-rotating vortices then spreads out slowly in the radial direction. On the other hand, for an upstream wind speed of 10 m/s (Fig. 14 (b)), the vortex pairs are formed at a larger downstream distance (y/d = 9). Similarly for upstream wind speeds of 13.1 m/s (Fig. 14 (c)) and 15.1 m/s (Fig. 14 (d)), the vortices are observed at even larger downstream distances of y/d = 12 and y/d = 14 respectively. From this comparative analysis, it can be concluded that the upstream wind speed is one of the major factors affecting the near-wake length; thus higher the wind speed, longer is the near-wake length. Therefore, the study of the wake instability as a function of the downstream distance is important and plays a pivotal role in the design of wind farms.

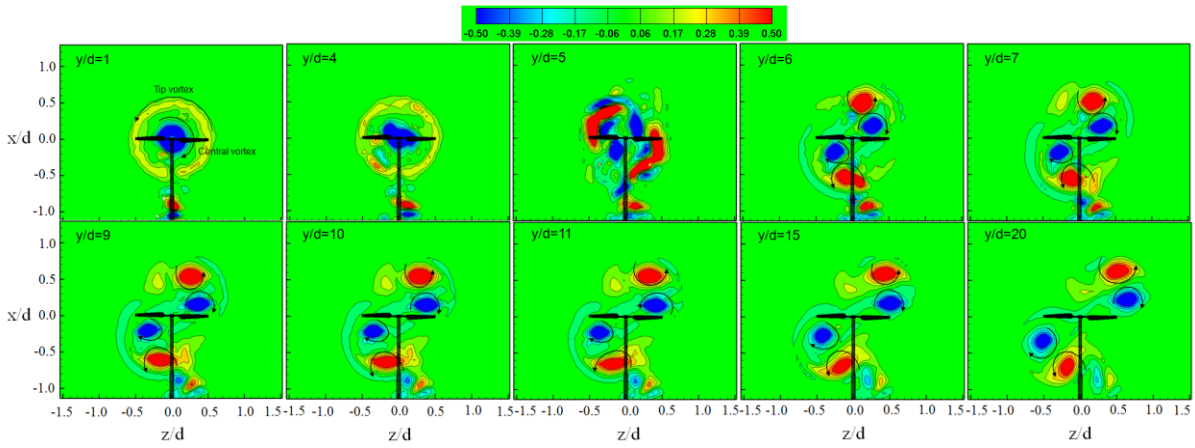

(a) Wind speed of 7m/s.

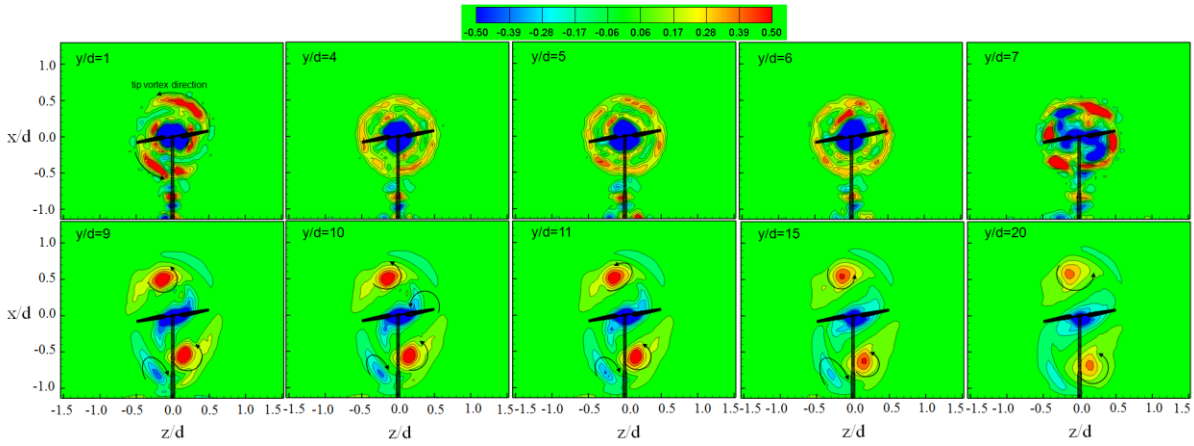

(b) Wind speed of 10m/s.

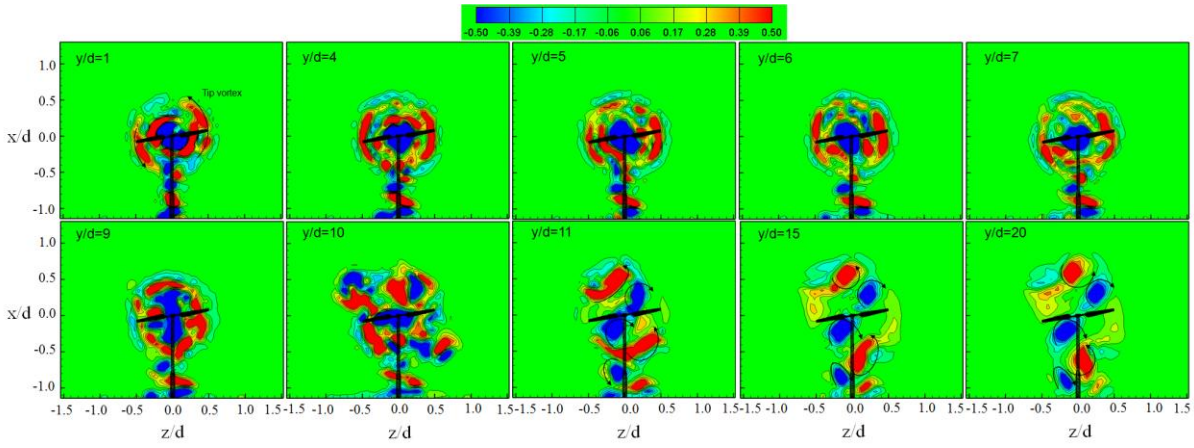

(b) Wind speed of 13.1m/s.

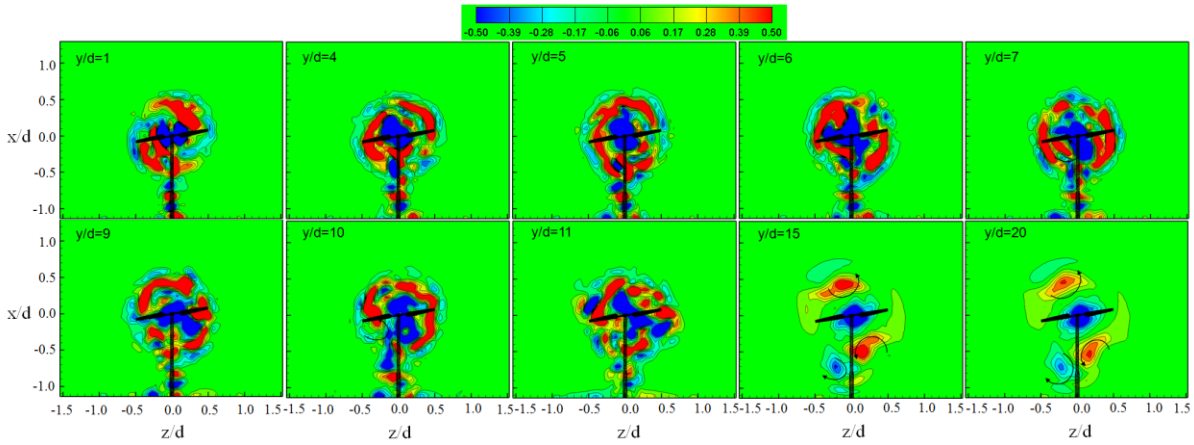

(c) Wind speed of 15.1m/s.

Fig. 14 Instantaneous y-vorticity at selected normalized axial locations for different wind speeds.

Fig. 15 (a) A field experiment at Risø test centre (b) NASA Ames (24.4m×36.6m) wind tunnel (Web References [1-2]).

The vorticity fields in Figure 14 illustrate the complexity of the wind turbine wake and its sensitivity to the wind speed. These patterns are further illustrated in Figure 16 by the combined instantaneous distributions of y-vorticity and velocity vectors at y/d = 20. For a wind speed of 7 m/s (Fig 14(a) and Fig 16(a)), the helical tip vortices are seen to form a tightly-wound helix which persists up to y/d = 4. The central blade root vortices are also seen to roll together form a strong axial vortex downstream of the hub. However, between y/d = 4 and y/d = 6 the flow structure undergoes a rapid breakdown whereby the helical structure breaks down to form a pair of well-defined streamwise

vortices and the root vortices move apart and away from the turbine axis. Downstream of y/d = 6 the structure appears to evolve into two distinct vortex pairs that move away from the turbine axis towards the top-right and bottom-left of the z-x sectional planes. Curiously, downstream of the breakdown zone the flow pattern undergoes very little rotation. Other features in this flow include a system of necklace vortices formed at the base of the tower and at the junction of the tower and the rotor hub-nacelle assembly. Downstream these vortices interact with the rotor tip vortices, although they do not seem to qualitatively alter the overall structure of the wake pattern. The vorticity and velocity patterns depicted in Figure 16(a) demonstrate that at y/d = 20 there is a significant level of interaction between the vortex pairs and the walls of the wind tunnel, seen through both the distance of the vortex cores from the wall compared with the core sizes, and the increased velocity of the near-wall flow adjacent to the vortices. These observations, combined with the apparent trajectories of these vortex pairs, suggest that their development is influenced by wall-confinement effects.

The case where the wind speed is 10 m/s is described in Fig 14(b) and Fig 16(b). The initial development is similar to the 7 m/s case, although the spiral is less tightly wound (as seen in Fig 14(b)). Similar to the lower speed case, the helical structure undergoes a breakdown between y/d = 6 and y/d = 9. Again, the helical structure of the tip vortices evolves rapidly into a pair of well-defined streamwise vortices. However, in this case, the root vortices remain tightly wound together at the turbine axis. Again, downstream of the breakdown zone the flow pattern does not undergo any overall rotation as the tip vortices appear to convect substantially along the vertical axis. Again, the proximity of the axial tip vortices to the tunnel walls at y/d = 20, as illustrated in Fig 16(b), suggests that confinement effects are present.

For the wind speed of 13.1 m/s the wake pattern's evolution, shown in Figs 14(c) and 16(c), is different again. In this case the vorticity distribution is more complex and less clearly defined, although it forms a reasonably consistent structure which persists up to y/d = 9. Between y/d = 9 and y/d = 11, the structure undergoes a transition to a pattern of streamwise vortices which bears some similarity to those in Figs 14(a) and 16(a), although less well defined. Here we observe the root vortices moving away from the turbine axis and forming two distinct longitudinal vortex pairs, as shown in detail in Fig 16(c). Some interaction also occurs between the lower axial vortex and the necklace vortices at the base of the tower. Again, the pattern appears to undergo no rotation and is likely to be affected by wall confinement.

Finally, for the case of 15.1 m/s wind speed, Figs 14(d) and 16(d), the wake forms a consistent, although complex structure which shows little evolution up to y/d = 10. From y/d = 10 to y/d = 15 the structure undergoes a transition to a pattern similar to Fig 14(b) and 16(b, whereby a single pair of tip vortices form and the root vortices remain at the turbine axis. Again, there is some interaction also between the lower axial vortex and the necklace vortices at the base of the tower. As for the two preceding cases, the axial vortices lie close to the vertical axis of symmetry with little rotation of the pattern. Interestingly, at y/d = 20 the uppermost axial vortex is further from the wind tunnel roof than in the preceding cases, which is probably due to the wake structure breakdown occurring further downstream in the 15.1 m/s case.

The complex behaviour described in Figures 14-16 is undoubtedly related to the circulation generated by the turbine blades, and this is related to the occurrence of stall. This has previously been illustrated in Figure 8 which demonstrates that in the case of the 7 m/s wind speed the blades are un-stalled. On the other hand, the blades are partially or completely stalled for the higher wind speed cases. The circulation of the root and tip vortices, and any in-between, generated by the turbine blades are related to the loading distributions along the blades, which will be different for each flow case. A more thorough analysis of this issue is, however, beyond the scope of the present paper.

Overall, the preceding vorticity patterns demonstrate that there is an interaction between the wake vortex structures and the walls of the wind tunnel. To determine whether this interaction is significant and whether the streamwise vortex patterns are present in practical flows, the structure needs to be investigated without wall confinement. Preliminary estimations can be obtained by implementation of zero-stress boundary conditions at the walls of the current mesh to generate some insight. However, this was not considered due to the scope of the present work. In addition, the influence of the walls of the tunnel on the initial flow development, where a helical vortex pattern is present, is unclear from the above results, and can be clarified by the proposed investigation.

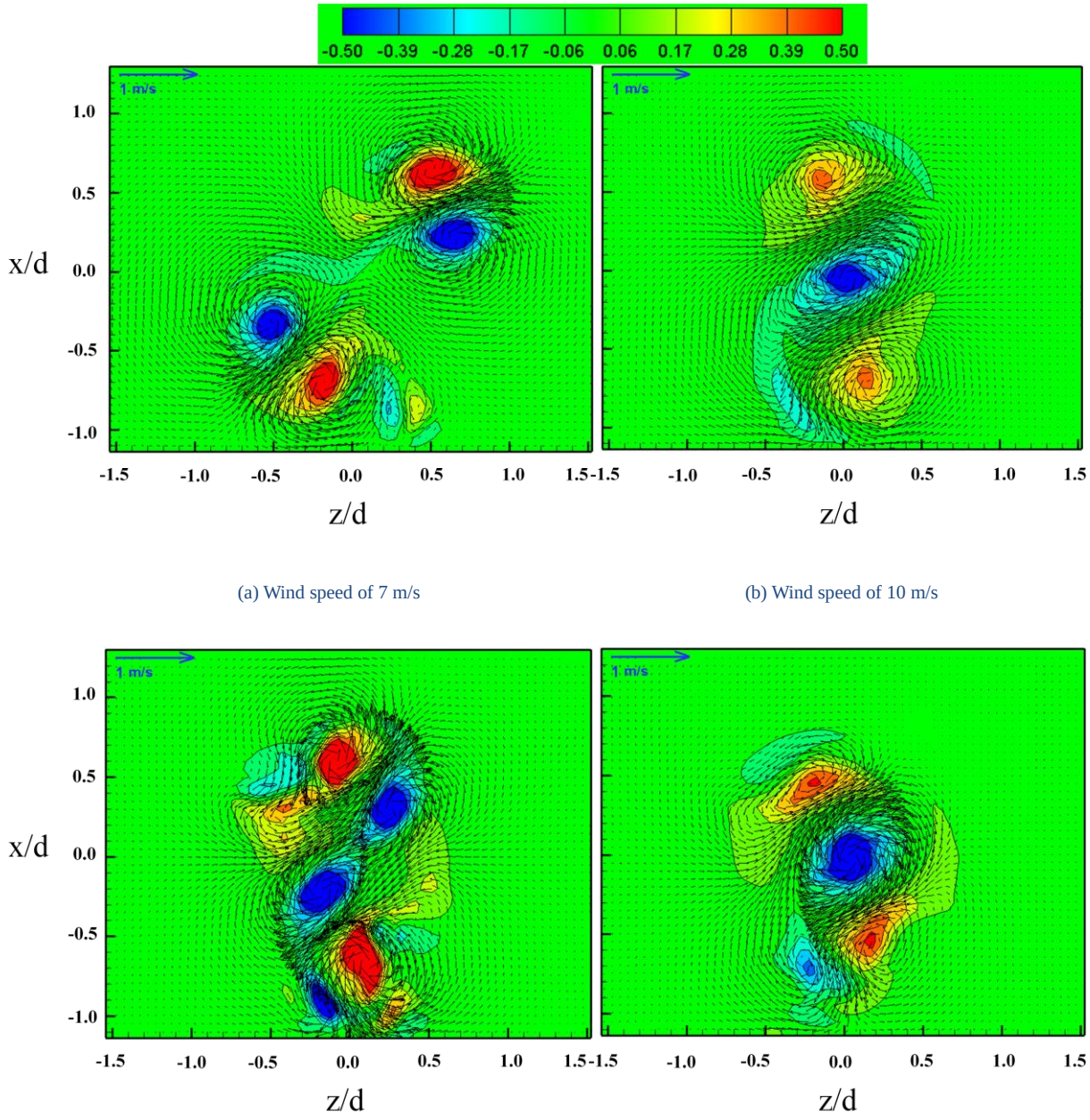

(a) Wind speed of 7 m/s

(b) Wind speed of 10 m/s

(c) Wind speed of 13.1m/s

(d) Wind speed of 15.1 m/s

Fig. 16 Overlapped instantaneous distribution of y-vorticity and velocity vectors in x and z directions at y/d=20.

3.4 Turbulence intensity and vortex breakdown

3.4.1 Comparison with a semi-empirical model

In addition to the shear-generated turbulence in the wake, the wind turbine itself generates additional turbulence, due to the tip vortices shed by the blades and the general distribution of the flow caused by the combined effects of the blades, nacelle and tower. Among these, the tip vortices are the dominant cause of TI increase in the wake because these set the basic dynamic behaviour of the wake as explained previously. In order to validate the average TI calculated from the LES, the results are compared with a semi-empirical model suggested by Hansen (2008). The semi-empirical model has been presented here for easy reference.

The turbulence in the wake (I_{wake}) is defined in terms of the added turbulence (I_+) and the ambient turbulence intensity (I_O) as:

$$I_{wake} = \sqrt{{I_O}^2 + {I_+}^2}$$

I_+ can be determined empirically using the following expression:

$$I_+ = 5.7{C_T}^{0.7}{I_O}^{0.68}\left(\frac{y}{y_n}\right)^{-0.96}$$

In the above equation, y is the downstream distance behind the wind turbine and y_n is the length of the near wake region. The length of the near wake, according to Vermeulen (1980) and taken from Burton (2001), is dependent on the rotor radius (R), the thrust coefficient and the wake growth rate (dr/dy) as:

$$y_n = \frac{nr_O}{\left(\frac{dr}{dy}\right)}$$

where

$$r_O = R\sqrt{\frac{m+1}{2}}$$

$$m = \frac{1}{\sqrt{1-\ C_T}}$$

$$n = \frac{\sqrt{0.214+0.144m}\left[1-\sqrt{0.134+0.124m}\right]}{\left(1-\sqrt{0.214+0.144m}\right)\sqrt{0.134+0.124m}}$$

The wake growth rate is given by

$$\frac{dr}{dy} = \sqrt{\left(\frac{dr}{dy}\right)_\alpha^2 + \left(\frac{dr}{dy}\right)_m^2 + \left(\frac{dr}{dy}\right)_\lambda^2}$$

In the above equation $\left(\frac{dr}{dy}\right)_\alpha$, $\left(\frac{dr}{dy}\right)_m$ and $\left(\frac{dr}{dy}\right)_\lambda$ are the growth rate contribution due to ambient turbulence, shear generated turbulence and the mechanical turbulence respectively and are given by:

$$\left(\frac{dr}{dy}\right)_\alpha = 2.5I_O + 0.005$$

$$\left(\frac{dr}{dy}\right)_m = \frac{(1-m)\sqrt{1.49+m}}{9.76(1+m)}$$

$$\left(\frac{dr}{dy}\right)_\lambda = 0.012\ B\ \lambda$$

The experimental thrust coefficient (C_T) for the wind turbine at a wind speed of 7 m/s was found to be 0.487. The ambient turbulence intensity (I_O), the tip speed ratio (λ) and the number of blades B are 0.2%, 5.41 and 2, respectively. Using the above empirical approach and the described inputs of the thrust coefficient and the ambient turbulence intensity, the TI in the wake is calculated and compared with the average TI for a wind speed of 7m/s, in Fig. 17. The turbulence intensities at y/d = 0.03 show the maximum values of 57.53% and 50.43% from the LES and the model, respectively. After this a sudden decrease to 10.34% for the LES and 1.74% for the model at y/d=1 are observed. The TI obtained using the semi-empirical model then stays approximately constant until y/d = 20, whereas the TI from the LES starts to increase until y/d = 3 and then decreases to y/d = 6 due to wake instability and vortex breakdown. After this the TI from the LES also becomes approximately constant to y/d = 20. The TI from the LES results is found to be 2.3% at y/d = 20 and is still quite high when compared with the upstream TI of 0.2% (11.5 times). Comparing this with the TI of 0.22% obtained from the model shows that the TI in the far-wake has approximately reached the upstream value of TI. It can be observed that the wake effect remains noticeable even in the far wake at distances as large as y/d = 20, when the wind turbine is constrained by the wind tunnel. It is believed that the TI predictions made by the LES are more accurate as compared to those made by the semi-empirical model, especially in the near-wake regions of wake instability and ongoing vortex breakdown.

Comparisons of maximum turbulence intensities obtained from the LES immediately behind the blade tips at y/d = 0.3 with those determined from the semi-empirical model at the same location are presented for the various wind speeds in Fig. 18. As can be seen, the average TI from the LES and the one predicted by the model agree quite well, at least up to an upstream wind speed of 10m/s. However,

afterwards large discrepancies are observed between both. It is believed that these differences result from the relationship between wind speeds and the aerodynamic characteristics of the turbine blades, as mentioned in regards to Fig.7. Recall that the NREL Phase VI wind turbine is stall-regulated. Hence the blades are designed to stall at high wind speeds without any requirement for pitch action. The turbine therefore is divided into two operating states, pre-stall and post-stall. In this research, it was observed that the stall phenomenon occurs when the wind speed exceeds 10m/s, as shown in Fig. 7. At this wind speed, flow separation starts from the root regions of the blade and progresses towards the tip regions. The flow moves towards the tip under the influence of the centrifugal acceleration and the pressure gradients in the radial direction (Corten and Nederland, 2001; Mo and Lee, 2012). Therefore it was observed that the TI predicted using the semi-empirical model is a good fit, especially in the pre-stall state. However, as it can be seen, the semi-empirical model does not cater for the post-stall state.

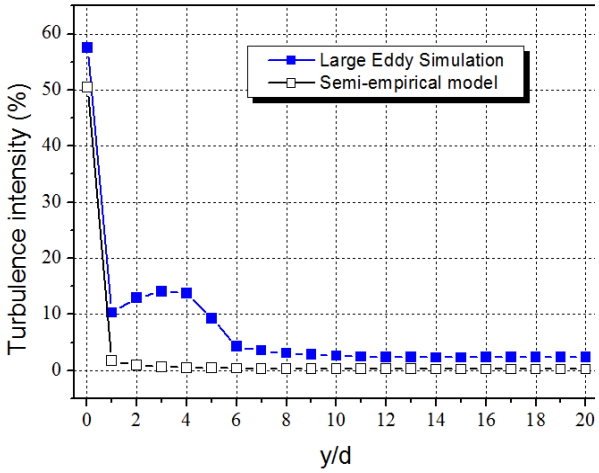

Fig. 17 Comparison of the average TI in LES with the semi-empirical model in the wake for a wind speed of 7m/s.

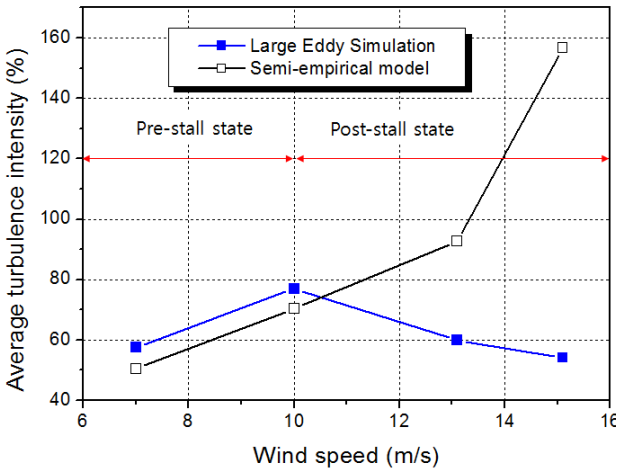

Fig. 18 Comparisons of average TI from the LES and the semi-empirical model for various wind speeds at y/d = 0.03.

3.4.2 Correlation between vortex breakdown and turbulence intensity

A comparison of average turbulence intensities for each of the wind speeds simulated in the current article as the downstream distance increases is presented in Fig. 19 (a). It can be observed that higher the wind speed, the larger is the maximum TI observed at y/d=0.03, just after the wind turbine. The TI of 42.57%, 45.31%, 54.12% and 63.32% are observed for correspondingly increasing wind speeds simulated in the article. The consequent increase in the average turbulence intensities immediately downstream of the turbine is primarily due to the stall experienced by the blades at higher wind speeds. The magnitude of flow separation immediately behind the turbine results in the corresponding increase of the TI. However, it is interesting to note that immediately afterwards the TI, for all cases, suddenly drops.

A magnified view of the enclosed region in Fig. 19 (a), corresponding to the region $2 < y/d < 20$, is shown in Fig. 19 (b). Here, it can be observed that after the initial decay of turbulence intensity, depending on the wind speed, the turbulence intensity either increases or remains approximately constant. This behaviour of the turbulence intensity, when correlated with the vorticity contours presented in Fig.14, indicates that the tightly wound spiralling vortices are the dominant features in the flow field. Interestingly, as these structures breakdown, a decrease in TI is observed. As observed in Fig. 19 (b), the corresponding downstream location for which the vortex breakdown and the decrease in TI occurs, depends on the upstream wind speed. Therefore for an upstream wind speed of 7 m/s, both the vortex breakdown and the TI decrease occur in the region $4 < y/d < 6$. Similarly for upstream wind speeds of 10 m/s, 13.1 m/s and 15.1 m/s, the corresponding downstream regions where vortex breakdown and decrease in TI is observed are $6 < y/d < 8$, $9 < y/d < 11$ and $11 < y/d < 13$ respectively. Therefore as the upstream wind speed increases, the TI propagates further downstream and decay is delayed.

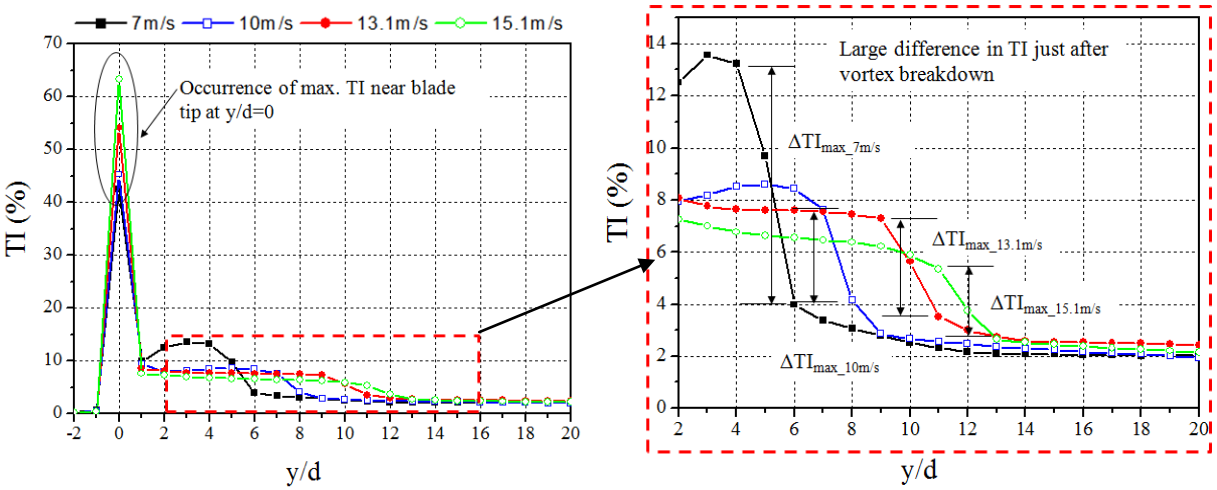

(a) Comparison of the average turbulence intensities for different wind speeds for each downstream location.

(b) An enlarged view of the region 2 < y/d < 20 from Fig. 18 (a).

Fig. 19 Turbulence intensities in the wake of the NREL Phase VI wind turbine for different wind speeds.

3.4.3 Wake length

The wake length is generally divided into two regions: near-wake and far-wake. The conventional definition of near wake, according to Vermeer et al. (2003), is the region immediately behind the wind turbine, and here the aerodynamics of the turbine is prevalent. On the other hand the far-wake region is where the effects of wind turbine aerodynamics are not visible. The division of the wake into these two zones has been revised in the current article based on the behaviour of the vortex structures in the wake and the dependency of the average TI on these structures. Therefore, the near wake has been defined as the region downstream of the wind turbine where the dominant flow structures are the tightly-wound, helical vortices originating from the tips and the hub. The near wake is the zone where the TI does not decay considerably. On the other hand, due to wake instability, the vortex structures finally breakdown, depending on the freestream wind speed. As a result, as depicted in Fig. 19, the resulting TI also drops. The region after the breakdown of the vortex structures has been defined as the far-wake region of the wind turbine wake.

Therefore, it will be useful for wind farm designers to be able to distinguish between the regions of stable wake, where vortex breakdown has not occurred, and the regions where the breakdown has already occurred. The relatively higher TI, in the near-wake, is likely to cause vibrations of the blades, adversely affecting the fatigue life of the tandem wind turbine operating in the far-wake. Hence a boundary between the near- and far-wake and its relationship with the wind speed will help the designers to efficiently design wind farms and determine the spacing between consecutive turbines based on average wind speeds. Through the detailed description of the vortex breakdown in the wake and the consequent drop of TI, a boundary between the near- and far-wake has been proposed and is presented in Fig. 20. It is suggested that the boundary can be defined as the average location between the starting and ending of the wake breakdown process. Fig. 20 provides simple guidelines for wind farm designers to efficiently reduce the effects of turbulence intensity on downstream wind turbines. Other factors of interest to the wind farm designers might include the mean and instantaneous velocity deficits and their relation with the vortex patterns observed in the wake as well as the frequency content of the wake that might give rise to buffeting forces due to dynamic stall on the downstream wind turbines. These factors are a possible avenue for future research.

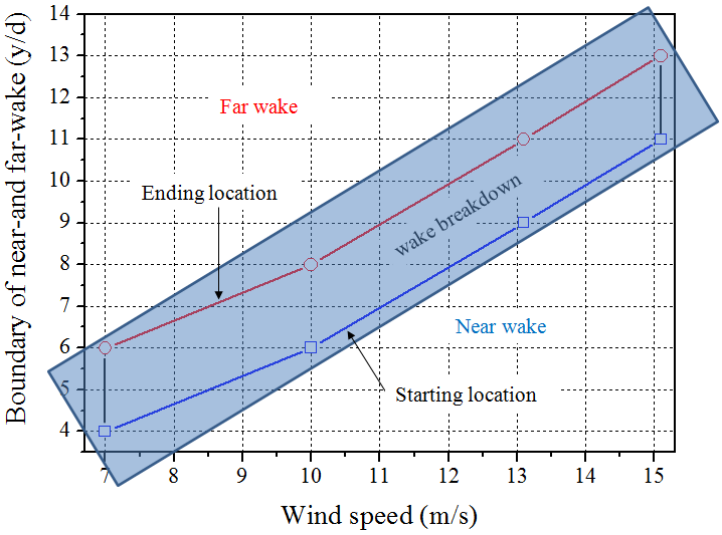

Fig. 20 Boundary of near-and far-wake as a function of wind speed.

4. Conclusions

A Large Eddy Simulation of NREL Phase VI wind turbine, with uniform inlet conditions, was carried out in order to analyze and better understand the turbulent characteristics of the wake, its instability and its consequent breakdown behind the wind turbine. The simulation was performed using a virtual wind tunnel model, having the same test section as that of the NASA Ames 24.4 m × 36.6 m tunnel. The reliability and validity of the analysis were verified using the experimental results released by NREL. Comparisons between the pressure coefficients and the average power for the various wind speeds considered showed a very good agreement between the numerical and the experimental results. Furthermore, the comparisons also showed that the LES results were in much better agreement with the experiments, as compared to the steady-state simulations of the two-equation turbulence models conducted by previous researchers, although the simulation times required were also significantly larger. The comparisons between the pressure coefficients and the wind turbine power output offer sufficient evidence that the predictions of the wake characteristics behind the wind turbine are reliable. The salient observations made as a consequence of this research are summarized as follows:

1) It was highlighted, based on the output power of the wind turbine, that the wind turbine operating states can be classified as pre-stall, transitional and post-stall states, depending on the flow state along the blade length. During the pre-stall state, the flow is largely attached to the blade surface whereas in the post-stall state, the flow is completely separated over the entire blade length. During the transitional state, the flow is attached near the tip regions and is separated near the root regions, as observed for wind speed of 10 m/s. It was shown that the flow structures in the wake largely depend on this operating state of the wind turbine.
2) W-shaped axial velocity profiles were observed downstream of the wind turbine at the station y/d = 1. It was observed that the momentum extraction from the upstream flow, and the hence the normalized velocity deficits, are a function of the upstream wind speed. The largest velocity deficits were observed in the wake of the wind turbine for the smallest wind speed and the deficit decreased as the wind speed was increased. It was observed that due to momentum recovery, with increasing distance downstream of the wind turbine, the velocity deficits decreased and ultimately formed V-shaped velocity profiles at a distance of eight rotor diameters downstream. However, the wake effects were still quite noticeable, and full velocity recovery was not seen, even in the far-wake at a distance of 20 rotor diameters.
3) It was observed that the wake behind the wind turbine consist of a system of intense and stable helical vortices generated by the turbine blades. These vortex structures in the wake become unstable, breaking down and forming patterns of streamwise vortices in the far wake. The location and streamwise extent of the breakdown increase as the upstream wind speed is increased, occurring between y/d = 4 and y/d = 6 at a wind speed of 7 m/s, and between y/d = 10 and y/d = 15 at a wind speed of 15.1 m/s. Downstream of the breakdown region, a system of streamwise vortices develops, with the detailed structure depending on the upstream wind speed, and being governed by the associated spanwise loading distribution of the turbine blades. An unexpected feature of the far wake pattern is the small rate of rotation exhibited by the vortex system as a whole. The proximity of the streamwise wake vortices to the tunnel walls suggests that there may be confinement effects in the far wake. It is also evident that the complex flow structures in the far wake are closely related to the local increase in the TI observed at those stations.
4) The TI in the wake of the wind turbine computed using LES was compared with an empirical model and very good agreement was observed between the two, especially in the far-wake. It was furthermore observed that the empirical model does not cater for the stalled wind turbine

blade and therefore only predicts the turbulence intensities in the pre-stall state.

5) The maximum TI generated at the blade tips quickly decayed until y/d = 1. After the initial large decay, the TI started to increase for the case of 7m/s whereas for the higher wind speed cases, it remained approximately constant. After this, a further decrease in TI was observed at different downstream stations, depending on the upstream wind speed. The second decrease in TI is closely related to the vortex breakdown and is observed at the distance where the primary vortex breakdown occurs. Therefore, it was observed that as the upstream wind speed increases, the TI remains high further downstream and the second decay is delayed. The maximum TI observed near the blade tips increases as the upstream wind speed is increased. The TI in the far-wake at y/d = 20 is still larger than that observed by the wind turbine itself and therefore will result in vibrations of the rotor blades of the tandem wind turbine which is operating in the wake.

6) Using the LES results, it was proposed that the boundary between the near and far-wake can be identified as the average location between the starting and ending of the vortex wake breakdown process. Therefore for upstream wind speeds of 7 m/s, 10 m/s, 13.1 m/s and 15.1 m/s, the boundary between the near- and far-wake lies at 5d, 7d, 10d and 12d respectively.

The information made possible due to this research can be used by wind farm designers to predict the relationship between the overall efficiency loss of a wind farm and distances between turbines inside the large wind farms. However, it is important to note that the relationship depends on parameters such as ambient turbulence intensity, wind speed and direction and the geographical features surrounding the wind farm as well as the individual turbine design such as the number of blades and the operational rpm. In the future, this relationship will be further explored by simulating a wind turbine in open environment and observing the flow structures in the unbounded wake.

References

Aderson, M.B., Milborrow, D.J., Ross, N.J., 1982. Performance and wake measurements on a 3m diameter horizontal axis wind turbine. Comparison of theory, wind tunnel and field test data, Technical report, University of Cambridge, Department of Physics, Cavendish Lab, Cambridge, U.K.

Ainslie, J.F., 1985. Development of an eddy viscosity model for wind turbine wakes. 7th BWEA Wind Energy Conference, Oxford, U.K., 61-66.

Ainslie, J.F., 1988. Calculating the flowfield in the wake of wind turbines. Journal of Wind Engineering and Industrial Aerodynamics 27, 213-224.

Barthelmie, R., Frandsen, S., Hansen, K., Schepers, J., Rados, K., Schlez, W., Neubert, A., Jensen, L., Neckelmann, S., 2009. Modelling the impact of wakes on power output at Nysted and Horns Rev, European Wind Energy Conference.

Barthelmie, R., Larsen, G., Frandsen, S., Folkerts, L., Rados, K., Pryor, S., Lange, B., Schepers, G., 2006. Comparison of wake model simulations with offshore wind turbine wake profiles measured by sodar. Journal of Atmospheric and Oceanic Technology 23, 888-901.

Burton, T., 2001. Wind Energy: Handbook. John Wiley & Sons, Ltd.

Chamorro, L.P., Porté-Agel, F., 2009. A wind-tunnel investigation of wind-turbine wakes: boundary-layer turbulence effects. Boundary-Layer Meteorology, 132, 129-149.

Corten, G.P., Nederland, E.C., 2001. Inviscid stall model. Netherlands Energy Research Foundation.

Crespo, A., Hernández, J., 1989. Numerical modelling of the flow field in a wind turbine wake, Proc. 3rd Joint ASCE/ASME Mechanics Conf. Forum on Turbulent Flows (ASME FED) pp 121–127..

Crespo, A., Manuel, F., Moreno, D., Fraga, E., Hernandez, J., 1985. Numerical analysis of wind turbine wakes. Proc. Delphi Workshop on Wind Energy Applications ed G Bergeles and J Chadjivassiliadis pp 15–25.

de Vries, O., 1979. Wind-tunnel tests on a model of a two-bladed horizontal axis wind turbine and evaluation of an aerodynamic performance calculation method. Technical report NLR TR 79071 L, NLR, Amsterdam, Netherlands.

Germano, M., Piomelli, U., Moin, P., Cabot, W.H., 1991. A dynamic subgrid-scale eddy viscosity model. Physics of Fluids A: Fluid Dynamics 3, 1760.

Gómez-Elvira, R., Crespo, A., Migoya, E., Manuel, F., Hernández, J., 2005. Anisotropy of turbulence in wind turbine wakes. Journal of Wind Engineering and Industrial Aerodynamics 93, 797-814.

Hand, M.M., Simms, D.A., Fingersh, L.J., Jager, D.W., Cotrell, J.R., Larwood, S.M., 2001 Unsteady Aerodynamics Experiment Phase VI: Wind Tunnel Test Configurations and Available Data Campaigns, NREL/TP-500-29955. National Renewable Energy Laboratory.

Hansen, M.O.L., 2001. Aerodynamics of wind turbines. Earthscan Publications Ltd.

Hau, E., 2010. Wind Turbines-Fundamentals, Technologies, Application, Economics. Springer.

Hinze, J., 1975. Turbulence, McGraw-Hill.

Ivanell, S., Sørensen, J., Henningson, D., 2007. Numerical computations of wind turbine wakes. Wind Energy, 259-263.

Jensen, N.O., 1983. A note on wind generator interaction. Risø National Laboratory.

Katic, I., Højstrup, J., Jensen, N., 1986. A simple model for cluster efficiency. European Wind Energy Association, 407-409.

Kim, S.-E., 2004. Large eddy simulation using unstructured meshes and dynamic subgrid-scale turbulence models. Technical Report AIAA-2004-2548. American Institute of Aeronautics and Astronautics, 34th Fluid Dynamics Conference and Exhibit.

Kraichnan, R.H., 1970. Diffusion by a random velocity field. Physics of Fluids, 13, 22.

Launder, B.E., Sandham, N.D., 2002. Closure strategies for turbulent and transitional flows. Cambridge Univ Press.

Lilly, D., 1992. A proposed modification of the Germano subgrid-scale closure method. Physics of Fluids A: Fluid Dynamics 4, 633.

Lissaman, P., 1977. Energy effectiveness of arrays of wind turbine conversion systems, Technical Report AV FR 7058. AeroVironment, Pasadena, California, USA.

Lissaman, P., Gyatt, G., Zalay, A., 1982. Numeric-modelling sensitivity analysis of the performance of wind-turbine arrays, Technical Report UC-60. AeroVironment, Passadena, California, USA.

Menter, F., Langtry, R., Völker, S., 2006. Transition modelling for general purpose CFD codes. Flow, turbulence and combustion 77, 277-303.

Mo, J.O., Lee, Y.H., 2011. Numerical simulation for prediction of aerodynamic noise characteristics on a HAWT of NREL phase VI. Journal of mechanical science and technology 25, 1341-1349.

Mo, J.O., Lee, Y.H., 2012. CFD Investigation on the aerodynamic characteristics of a small-sized wind turbine of NREL PHASE VI operating with a stall-regulated method. Journal of mechanical science and technology 26, 81-92.

Okulov, V.L., Sorensen, J., 2004. Instability of a vortex wake behind wind turbines. Doklady Physics, Springer, pp. 772-777.

Potsdam, M.A., Mavriplis, D.J., 2009. Unstructured mesh CFD aerodynamic analysis of the NREL Phase VI rotor. AIAA Paper 2009-1221, AIAA Aerospace Sciences Meeting, Orlando FL.

Sanderse, B., 2009. Aerodynamics of wind turbine wakes. Energy research Centre of the Netherlands, ECN-E-09-016.

Shimizu, Y., Kamada, Y., 2001. Studies on a horizontal axis wind turbine with passive pitch-flap mechanism (performance and flow analysis around wind turbine). Journal of Fluids Engineering 123, 516.

Simms, D.A., 2001. NREL unsteady aerodynamics experiment in the NASA-Ames wind tunnel: A comparison of predictions to measurements. National Renewable Energy Laboratory.

Simms, D.A., Schreck, S., Hand, M., Fingersh, L.J., 2001. NREL unsteady aerodynamics experiment in the NASA-Ames wind tunnel: A comparison of predictions to measurements, NREL/TP-500-29494. National Renewable Energy Laboratory.

Smagorinsky, J., 1963. General circulation experiments with the primitive equations 1. The basic experiment. Monthly Weather Review, 91, 99-164.

Smirnov, A., Shi, S., Celik, I., 2001. Random flow generation technique for large eddy simulations and particle-dynamics modeling. Journal of Fluids Engineering, 123, 359.

Sørensen, N.N., Michelsen, J.A., Schreck, S., 2002. Navier–Stokes predictions of the NREL phase VI rotor in the NASA Ames 80 ft × 120 ft wind tunnel. Wind Energy, 5, 151-169.

Vermeer, L., Sørensen, J.N., Crespo, A., 2003. Wind turbine wake aerodynamics. Progress in Aerospace Sciences, 39, 467-510.

Vermeulen, P., 1980. An experimental analysis of wind turbine wakes, Proceedings of the International Symposium on Wind Energy Systems, Lyngby, Denmark, 431-450.

Vermeulen, P., Builtjes, P., Vijge, J., 1981. Mathematical modelling of wake interaction in wind turbine arrays, Part 1. report TNO, 81-01473.

Wagner, S., Bareiss, R., Guidati, G., 1996. Wind turbine noise, Springer-Verlag.

Wu, Y.T., Porté-Agel, F., 2011. Large-eddy simulation of wind-turbine wakes: evaluation of turbine parametrisations. Boundary-Layer Meteorology 138, 345-366.

Web references

[1] http://www.nrel.gov/ , Access date: 15-10-2011

[2] http://www.risoe.dtu.dk/, Access date: 15-10-2011